Pacific Northwest
NATIONAL LABORATORY

PNNL-38197

Evaluating High-Halide Waste Form Options for Salt-Based Nuclear Waste Simulants

September 2025

Jincheng Bai
Harmony S. Werth
Brian J. Riley
Miroslava Peterson

U.S. DEPARTMENT OF ENERGY

Prepared for the U.S. Department of Energy
under Contract DE-AC05-76RL01830

DISCLAIMER

PACIFIC NORTHWEST NATIONAL LABORATORY
operated by
BATTELLE
for the
UNITED STATES DEPARTMENT OF ENERGY
under Contract DE-AC05-76RL01830

Printed in the United States of America

Available to DOE and DOE contractors from
the Office of Scientific and Technical Information,
P.O. Box 62, Oak Ridge, TN 37831-0062
www.osti.gov
ph: (865) 576-8401
fox: (865) 576-5728
email: reports@osti.gov

Available to the public from the National Technical Information Service
5301 Shawnee Rd., Alexandria, VA 22312
ph: (800) 553-NTIS (6847)
or (703) 605-6000
email: info@ntis.gov
Online ordering: http://www.ntis.gov

PNNL-38197

Evaluating High-Halide Waste Form Options for Salt-Based Nuclear Waste Simulants

September 2025

Jincheng Bai
Harmony S. Werth
Brian J. Riley
Miroslava Peterson

Prepared for
the U.S. Department of Energy
under Contract DE-AC05-76RL01830

Pacific Northwest National Laboratory
Richland, Washington 99354

Executive Summary

In this study, waste forms were being explored for an electrochemical salt simulant, , referred to as ERV3, which is a high-LiCl/KCl salt containing simulated fission products (i.e., Sr, Cs, Nd) and Na to represent bond sodium from Experimental Breeder Reactor-II metallic fast reactor fuel. The goal was to find glassy systems that could be used to immobilize the salt in a single-step process. The envisionment of this process would be to find a frit glass that could be added to the salt waste, heat treated, poured into waste canisters, and then stored for disposal. To perform this study, a literature review was conducted. Then the most promising seven systems were fabricated without the ERV3 salt simulant and then mixed with salt simulant and heat treated under different processes (see Table S1). The criteria that were used to screen potential compositions included demonstrated alkali incorporation, could be melted at reasonably low temperature ($T \leq 1000°C$), and if the compositions had some demonstrated data for waste-form-related properties, that was a benefit. High marks were given for compositions that showed amorphous nature after slow cooling of samples containing ERV3.

Table S1. Summary of glass and salt-loaded glass prepared broken out by set, sample ID, glass composition, salt loading, and heat-treatment method.

Set	Sample ID	Nominal Glass Composition (mol%)	ERV3 Salt Loading (mass%)	Heat-Treatment Method
A	Fe-P	$40Fe_2O_3$-$60P_2O_5$	0	Melt-quench
	Fe-P-0ERV3-F	$40Fe_2O_3$-$60P_2O_5$	0	Furnace cool
	Fe-P-10ERV3-F	$40Fe_2O_3$-$60P_2O_5$	10	Furnace cool
	Fe-P-20ERV3-F	$40Fe_2O_3$-$60P_2O_5$	20	Furnace cool
B	Zn-Bi-Si	$20ZnO$-$40Bi_2O_3$-$40SiO_2$	0	Melt-quench
	Zn-Bi-Si-10ERV3-Q	$20ZnO$-$40Bi_2O_3$-$40SiO_2$	10	Melt-quench
	Zn-Bi-Si-10ERV3-F	$20ZnO$-$40Bi_2O_3$-$40SiO_2$	10	Furnace cool
C	Zn-Bi-B-1	$25ZnO$-$15Bi_2O_3$-$60B_2O_3$	0	Melt-quench
	Zn-Bi-B-1-10ERV3-Q	$25ZnO$-$15Bi_2O_3$-$60B_2O_3$	10	Melt-quench
	Zn-Bi-B-1-10ERV3-F	$25ZnO$-$15Bi_2O_3$-$60B_2O_3$	10	Furnace cool
D	Zn-Bi-B-2	$25ZnO$-$50Bi_2O_3$-$25B_2O_3$	0	Melt-quench
	Zn-Bi-B-2-10ERV3-Q	$25ZnO$-$50Bi_2O_3$-$25B_2O_3$	10	Melt-quench
	Zn-Bi-B-2-10ERV3-F	$25ZnO$-$50Bi_2O_3$-$25B_2O_3$	10	Furnace cool
E	Mo-Bi-Te-1	$20MoO_3$-$2.5Bi_2O_3$-$77.5TeO_2$	0	Melt-quench
	Mo-Bi-Te-1-10ERV3-Q	$20MoO_3$-$2.5Bi_2O_3$-$77.5TeO_2$	10	Melt-quench
	Mo-Bi-Te-1-10ERV3-F	$20MoO_3$-$2.5Bi_2O_3$-$77.5TeO_2$	10	Furnace cool
F	Mo-Bi-Te-2	$20MoO_3$-$5Bi_2O_3$-$75TeO_2$	0	Melt-quench
	Mo-Bi-Te-2-10ERV3-Q	$20MoO_3$-$5Bi_2O_3$-$75TeO_2$	10	Melt-quench
	Mo-Bi-Te-2-10ERV3-F	$20MoO_3$-$5Bi_2O_3$-$75TeO_2$	10	Furnace cool
G	Mo-Bi-Te-3	$20MoO_3$-$10Bi_2O_3$-$70TeO_2$	0	Melt-quench
	Mo-Bi-Te-3-10ERV3-Q	$20MoO_3$-$10Bi_2O_3$-$70TeO_2$	10	Melt-quench
	Mo-Bi-Te-3-10ERV3-F	$20MoO_3$-$10Bi_2O_3$-$70TeO_2$	10	Furnace cool

Acknowledgments

Pacific Northwest National Laboratory (PNNL) is operated by Battelle Memorial Institute for the DOE under contract DE-AC05-76RL01830. This work was funded by the Department of Energy Office of Nuclear Energy under the Material Recovery and Waste Form Development Campaign (MRWFD, i.e., NE-43) within the Nuclear Fuel Cycle and Supply Chain (NFCSC) Program. Authors express thanks to Saehwa Chong (PNNL) for help with dilatometry as well as Melissa Rose, Levi Gardner, and William Ebert of Argonne National Laboratory (ANL) for providing the ERV3 salt and providing additional support for this work. Chemical durability testing was performed at ANL by William Ebert and Yifeng Liao but was not completed before this report was completed so that data will be discussed in follow-up report by ANL, likely to come out in the fall of 2025.

Acronyms and Abbreviations

ADP	ammonium dihydrogen phosphate
AL	analytical laboratory
ANL	Argonne National Laboratory
AQ	after quenching
ASTM	American Society for Testing and Materials International
DU	depleted uranium
EBR-II	Experimental Breeder Reactor-II (at Idaho National Laboratory)
ER(SF)	electrorefiner salt from Steve Frank (formerly of Idaho National Laboratory)
ERV3	electrorefiner salt (simulant) version 3
FY	fiscal year
G	glass
GBS-CWF	glass-bonded sodalite ceramic waste form
H	hygroscopic
HALEU	high-assay low-enriched uranium
HEU	highly enriched uranium
HT	heat treatment
ID	identification
IG	immiscibility gap
MIG	metastable immiscibility gap
Mk-IV	Mark-IV electrorefiner
Mk-V	Mark-V electrorefiner
MRWFD	Material Recovery and Waste Form Development (Campaign)
OR	oxide reduction
PCT	product consistency test
PNNL	Pacific Northwest National Laboratory
SEM	scanning electron microscopy
SIMS	secondary ion mass spectrometry
t	heat treatment time
T	heat treatment temperature
TEM	transmission electron microscopy

TGA	thermogravimetric analysis
TSC	Thermo Scientific Chemicals
U.S. DOE	United States Department of Energy
XRD	X-ray diffraction
XRF	X-ray fluorescence

Contents

Figures

Tables

1.0 Introduction

The United States Department of Energy (U.S. DOE) is investigating waste form options for immobilizing salt-based wastes that are generated during used nuclear fuel processing and reprocessing. The focus of this report is on the salt wastes from electrochemical reprocessing of used nuclear fuel, namely Experimental Breeder Reactor-II (EBR-II) fuel. Electrochemical reprocessing involves several steps including (1) chopped fuel dissolution within a molten salt (i.e., LiCl-KCl eutectic salt), (2) *actinide drawdown* through electrowinning where actinides are reduced and removed from the salt bath at a cathode for extraction, (3) *lanthanide drawdown* through electrowinning whereby lanthanides are selectively removed using the same process as actinide drawdown, (4) cathode processing, and (5) waste treatment for disposal. As shown in Figure 1-1 (Fredrickson 2021), several additional steps are involved in this process from start to finish. The purpose of the work described within this report was to document the rationale for the high-halide compositions selected for fabrication and characterization.

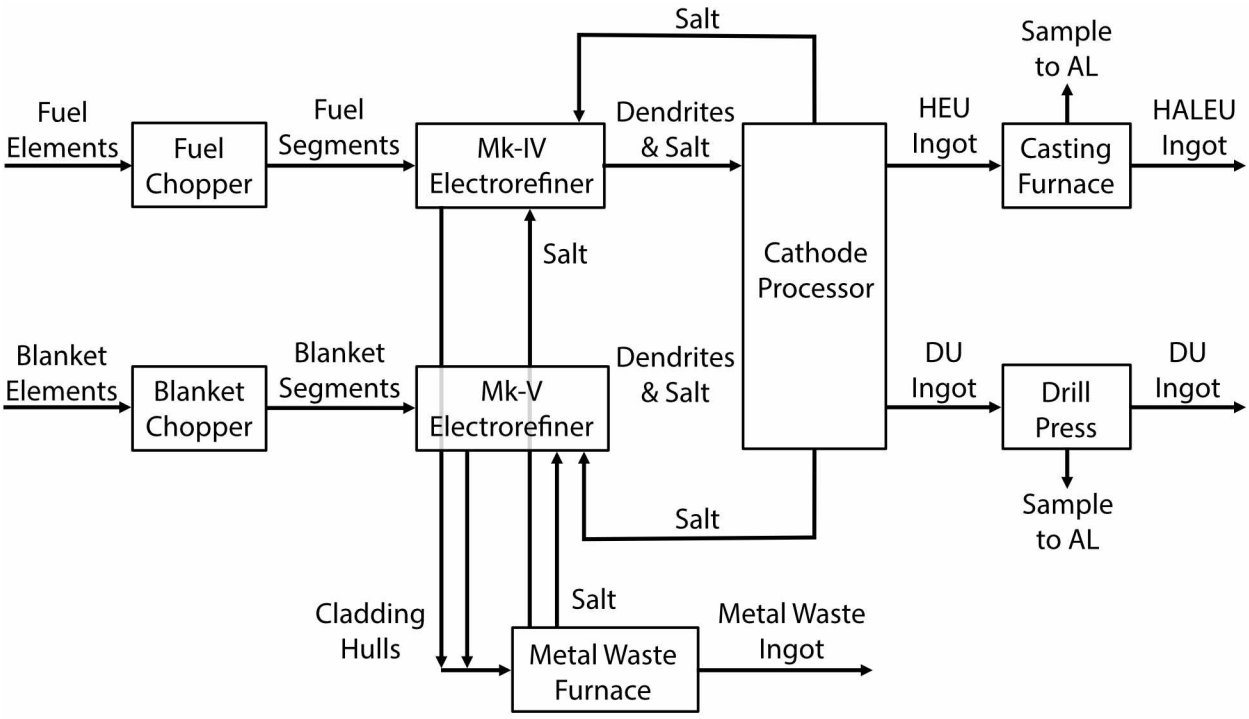

Figure 1-1. A summary of electrometallurgical processing within the U.S. DOE National Laboratory Complex from 1996–present. Within this diagram, AL denotes analytical laboratory, Mk-IV and Mk-V denote the Mark-IV and Mark-V electrorefiners, respectively, HALEU denotes high-assay low-enriched uranium, HEU denotes high-enriched uranium, DU denotes depleted uranium. This figure comes from Fredrickson (2021).

The driver for this work is to compare the results with the baseline technology for full-salt waste forms, which is the glass-bonded sodalite ceramic waste form (GBS-CWF) (Moschetti et al. 2000; Ebert 2005). The GBS-CWF is a heterogeneous waste form that contains sodalite crystals embedded within a glassy matrix where the Cl and some alkali metals incorporate into sodalite and the rest of the salt cations (i.e., Li, K) and fission products (e.g., Cs, Sr, rare earths) incorporate into the glassy phase. An example of the appearance and microstructure of GBS-CWF is provided in Figure 1-2 (Riley et al. 2017b). While the baseline GBS-CWF process requires

powder processing within a hot cell along with several independent experimental steps (i.e., V-blender mixing, salt occlusion, high-temperature pressureless sintering), steps are being made in 2024-2025 to evaluate methods for simplifying this process. However, even with several improvements to the GBS-CWF fabrication process, ultimate (theoretical) waste loading capacity in this waste form will remain limited due to the Cl loading restriction into sodalite [i.e., $Na_8(AlSiO_4)_6Cl_2$].

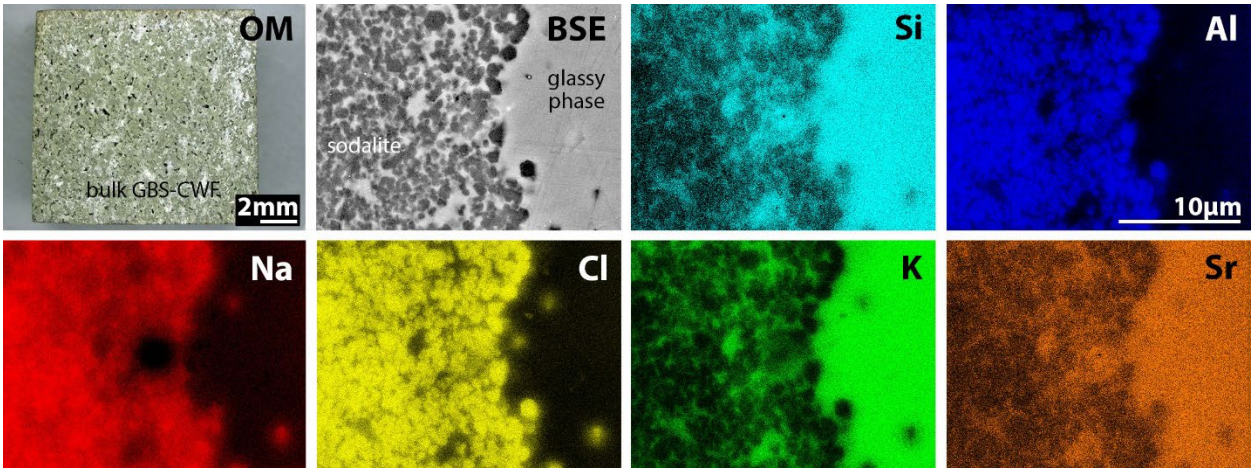

Figure 1-2. Pictures, scanning electron micrographs (SEM), and energy dispersive X-ray spectroscopy (EDS) elemental dot maps for 26N5-11 GBS-CWF documented in previous work by Riley et al. (2017b) This figure shows bulk appearance as well as the microstructure and microchemistry of the glass-sodalite interface.

An option for improving waste loading for GBS-CWF would be utilizing a glass binder that can accommodate additional Cl after the sodalite becomes fully loaded, but this is not currently being explored. With these things in mind, for comparison, all the glass systems evaluated in the current study all have higher waste loadings than the baseline GBS-CWF, which is ≈ 7–8 mass% salt, on a mass basis. The salt loading can be increased past this limit, but it results in residual NaCl crystals within the samples as shown in Figure 1-3 (Riley et al. 2017b).

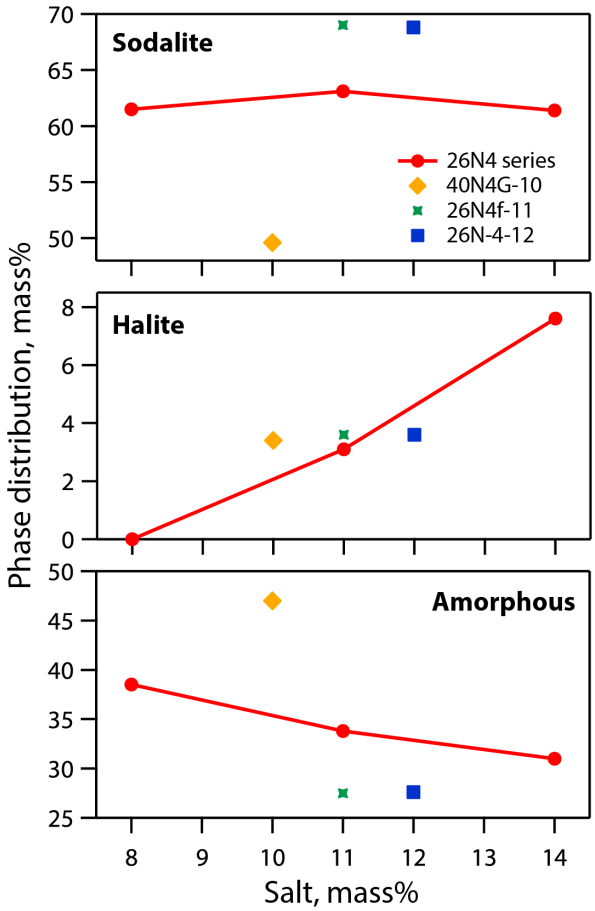

Figure 1-3. Phase distribution trends from X-ray diffraction for the NBS-4 sample series. The red circles include samples ACWF-26N4-8 (8 mass%), ACWF-26N4-11 (11 mass%), and ACWF-26N4-14 (14 mass%). This shows how residual halite (NaCl) is found in samples at waste loadings >8 mass%. This figure comes from Riley et al. (2017b).

2.0 Literature Review of Potential Glass Systems

This section provides an overview of the different types of glasses that are being considered. They include an overview of tellurite (TeO_2) glasses (Section 2.1), zinc bismuth (ZnO-Bi_2O_3) glasses (Section 2.2), and phosphate (P_2O_5) glasses (Section 2.3).

2.1 Tellurite Glasses

2.1.1 Oxyhalide Tellurite Glass

Family of oxychloride tellurite glasses was studied on the glass formation region across ternary compositional space (Kozhukharov et al. 1983). The batches were melted in quartz crucible between 800–1000°C. Special melting process was applied to reduce the volatility of halide-modified compositions, yet details cannot be retrieved. Promising systems with good forming region includes $x$$TeO_2$-(100-$x$)[$50P_2O_5$-$50BaCl_2$], $x$$TeO_2$-(100-$x$)[$50P_2O_5$-$50PbCl_2$] are shown in Figure 2-1, and the latter one has broader compositional surface for homogenous glass formation. Another ternary system of TeO_2-B_2O_3-PbF_2 has a large immiscibility gap on the B_2O_3 rich part (> 0.7) and good glass forming region on the low B_2O_3 part (< 0.3). Other interesting oxyhalide glass formation systems are: TeO_2-$NaPO_3$-$BaCl_2$ ($BaCl_2$ < 0.2), TeO_2-$Pb(BO_2)_2$-$BiCl_3$ (TeO_2 > 0.6), TeO_2-$Ba(PO_3)_2$-$BaCl_2$·P_2O_5.

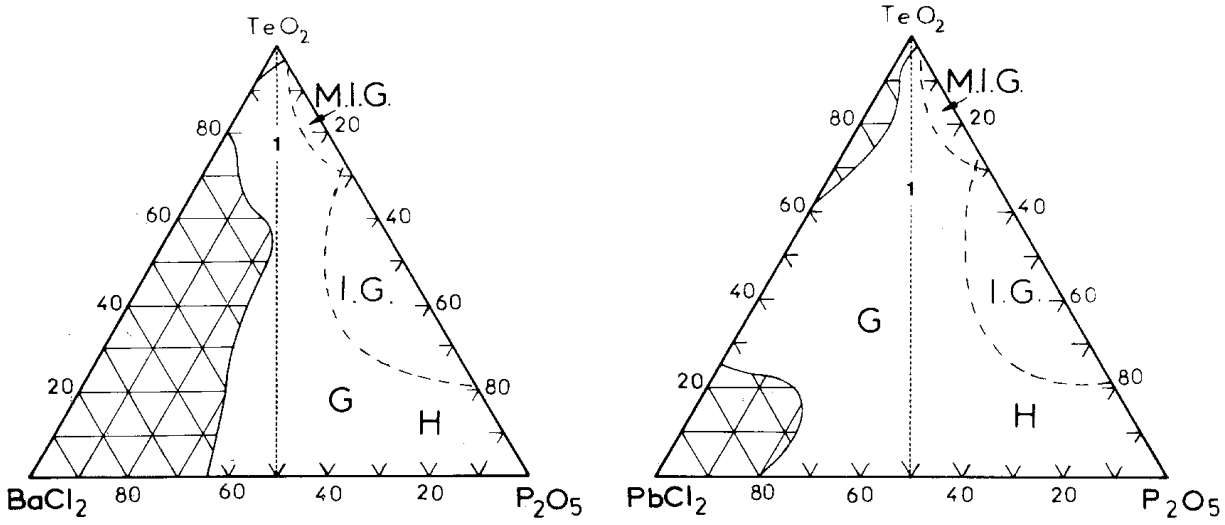

Figure 2-1. Ternary diagram demonstrating the glass forming region of TeO_2-P_2O_5-$BaCl_2$ (left) and TeO_2-P_2O_5-$PbCl_2$ (right) system. G is glass, IG is immiscibility gap, MIG is metastable immiscibility gap, and H suggest high hygroscopic nature on P_2O_5 rich end (Kozhukharov et al. 1983).

The glass forming region was studied in the LiCl-Li_2O-TeO_2 glasses (Tanaka et al. 1988), and the region is broadened toward the LiCl rich side as compared to the Li_2O rich side as shown in Figure 2-2. Binary LiCl-TeO_2 glass can be made with up to 60 mol% of LiCl. Glasses were fabricated with the chemicals of LiCl, Li_2CO_3 and β-TeO_2, and the batch was melted in a platinum crucible at 650°C to 800°C for 15 to 30 minutes in air. The melt was quenched by being pressed between iron plates. The glass transition temperature increased with the increasing amount of TeO_2 in glass. In another study, the LiX-Li_2O-TeO_2 and AgX-Ag_2O-TeO_2 (X = Cl, Br, I) glasses were prepared (Hase et al. 1995). It was noted that the binary systems of AgX-TeO_2 and LiX-TeO_2 as

well as the ternary system of LiI-Li_2O-TeO_2 failed to produce homogeneous bulk glasses. The powder mixture (~10 g) was melted in alumina crucibles at 700–1000°C in air for 10–20 minutes. Then, the melts were quenched to room temperature by sandwiching with iron plates. No technique was mentioned in determining the amorphous state of the glass. Glasses with chemical compositions of $y$$Li_2Cl_2-25Li_2O$-(75-$y$)$TeO_2$ (y = 5. 10, 15) and $z$$Ag_2Cl_2-25Li_2O$-(75-$z$)$TeO_2$ (z = 5, 10, 15) were prepared and tested for optical properties (transmittance and refractive index).

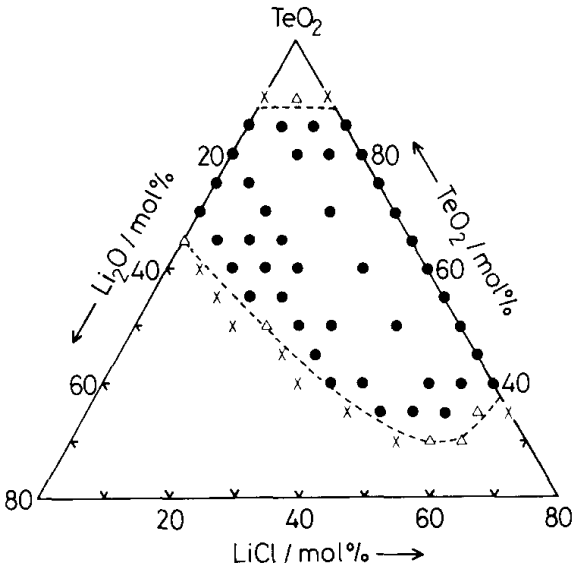

Figure 2-2. Glass forming region of the ternary LiCl-Li_2O-TeO_2 system. Solid circle is glass, open triangle is partly crystallized sample, and cross is crystallized sample (Tanaka et al. 1988).

The couple of AgI-Ag_2O was originally discovered with high ion conductivity in the vitreous state and later studies tested the glass forming ability in ternary systems with various oxides (e.g. TeO_2, MoO_3, and V_2O_5). The homogeneous incorporation of AgI in these glass systems shows potential applications for waste immobilization of iodine. Several tellurite glass systems were studied for the retention of AgI and the additions of Bi_2O_3, WO_3, MoO_3, and V_2O_5 aim to improve the chemical durability (Lee et al. 2017; Kang et al. 2021; Shin et al. 2024). These glasses were melted between 700 to 850°C for 20–60 minutes. X-ray fluorescence (XRF) showed that the retention of iodine ranged 86.2–100 mass%. The chemical durability of the glasses was characterized using the product consistency test (PCT) method (ASTM C1285) and the normalized leaching data by elements are compared in Table 2-1. The single glass made with Bi_2O_3 showed a higher leaching rate of iodine than glasses added WO_3, MoO_3, and V_2O_5 at similar additive level.

Table 2-1. Elemental leaching rates of AgI-Ag_2O-TeO_2 glass added with various oxides from the PCT.

Glass composition (mol%)	Normalized Release (g/m^2)			
	Te	I	Ag	Additive
19AgI-23Ag_2O-53TeO_2-5Bi_2O_3	3.90E-02	6.50E-04	8.0E-05	3.0E-05
18AgI-22Ag_2O-50TeO_2-10WO_3	7.39E-02	4.41E-06	8.18E-05	1.34E-01
18AgI-22Ag_2O-50TeO_2-10MoO_3	3.56E-02	4.42E-06	3.72E-04	2.42E-01
18AgI-22Ag_2O-50TeO_2-10V_2O_5	5.54E-02	8.59E-06	2.57E-05	1.52E-01

For the (x)Additive-(1-x)(0.20AgI-0.25Ag_2O-0.55TeO_2) glass system (additive = WO_3, MoO_3, V_2O_5), x = 0.10, increasing the amount of additive in glass reduced the leaching rate of tellurium and iodine. The lowest leaching rate of tellurium and iodine were found with glasses with the highest amount of additive (shown in Table 2-1). Furthermore, the effect of AgI on chemical durability was studied in the (x)AgI·(1−x)[(y)Ag_2O·(1−y)((z)WO_3·(1−z)TeO_2)] glass system. Four glass series were prepared with (1) y = 0.3 and z = 0.5, (2) y = 0.3 and z = 0.6, (3) y = 0.4 and z = 0.5, and (4) y = 0.4 and z = 0.6. Within each series, the x values are 0, 0.1, 0.2, 0.3, and 0.4. The structure of the glass was studied using X-ray photoelectron spectroscopy to characterize the elements constituting the glass matrix. The results showed no significant change in the bonding state and/or oxidation number with the addition of AgI up to 40 mol%. The compositional dependence of elemental leaching behavior was tested, and the results can be summarized as follows:

- For all glass series, the normalized release of Ag generally decreased with the increasing concentration of AgI. This was attributed to the better chemical stability of AgI than Ag_2O and the enrichment of AgI on the surface of glass.
- Higher fraction of Ag_2O or WO_3 in glass result in higher normalized release of I due to the partial reduction of Ag and W.
- The increased content of Ag_2O in glass prompted the normalized release of W, and it is potentially caused by Ag precipitation.
- The normalized release of Te increased with increasing AgI content. This was explained based on the mutual repulsion in the I ions with the lone pairs of TeO_3 and/or TeO_4.

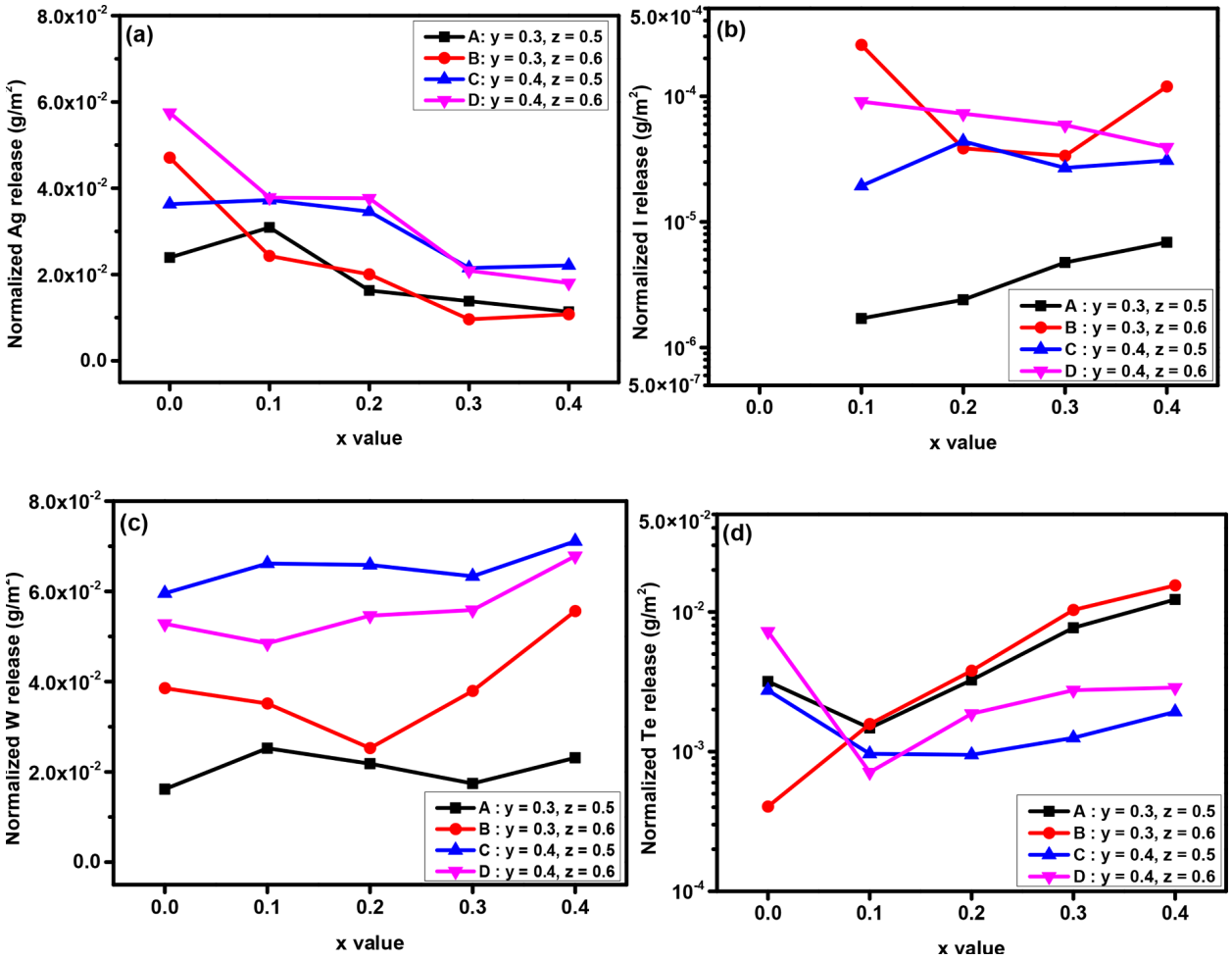

Figure 2-3. Elemental leaching of $(x)AgI\cdot(1-x)[(y)Ag_2O\cdot(1-y)<(z)WO_3\cdot(1-z)TeO_2>]$ glass system (Shin et al. 2024).

2.1.2 Lead Tellurite Glass

The binary $PbO\text{-}TeO_2$ system has a glass forming range with PbO = 5%- 24% in mass fraction. Glasses with 16%, 18%, 20% 22% (by mass) of PbO were prepared and the ones with PbO < 22 mass% were found highly crystallized and volatilizing during melting (Riley et al. 2017a). The $22PbO\text{-}78TeO_2$ (mass%) glass was selected to study the glass structure, the waste loading of chloride salt simulant, and the chemical durability (Riley et al. 2010; Riley et al. 2012). Among several candidate oxide tellurite glass systems (PbO, Al_2O_3+B_2O_3, WO_3, P_2O_5, or ZnO) during the scoping experiment, this $22PbO\text{-}78TeO_2$ glass showed the best chemical durability in terms of sodium leaching in PCT test under the same waste salt loading (10 mass%).

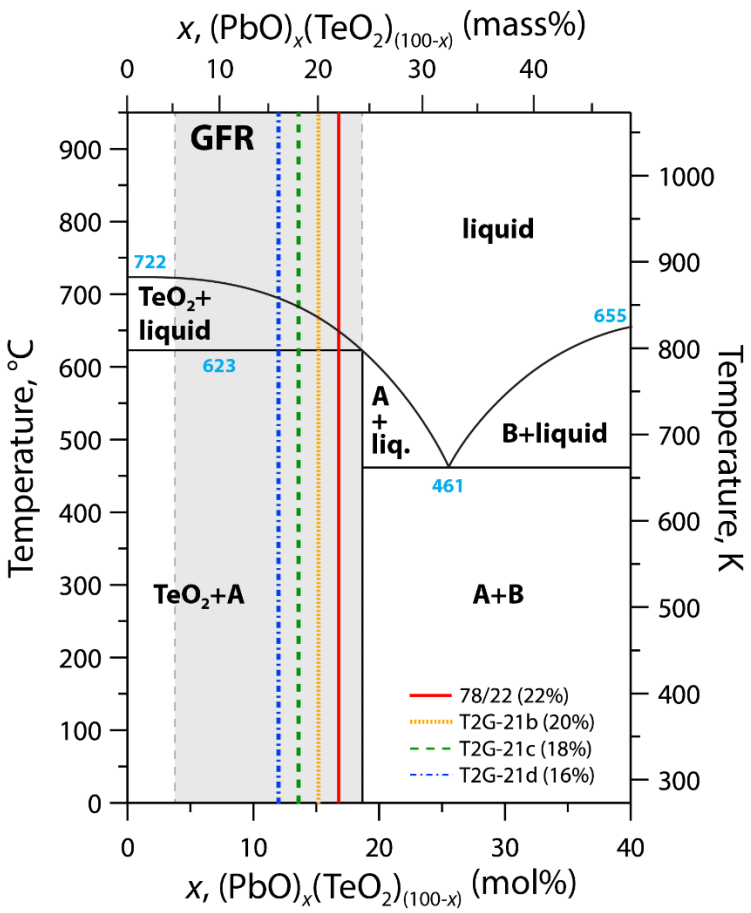

Figure 2-4 Binary phase diagram of PbO-TeO_2 system with glass forming region indicted in grey color (Riley et al. 2017a).

The loading limit of salt waste simulant was characterized, and the clear glassy state was achieved up to 14 mass% of salt mixture loaded (McCloy et al. 2013) (see Figure 2-5) (Riley et al. 2017a). Higher amount of salt in glass results in the opaque appearance of sample that is caused by phase separation between a TeO_2/PbO-rich phase and a crystalline phase rich in alkali chlorides. The NMR analysis on the glass structure constituent showed little impact on the Te speciation with the addition of salt. The salt additives were more likely to be accommodated by the Pb species as evidenced by the monotonical change between the relative concentration of two Pb species with the addition of mixed chlorides. The Na and Cl ions are incorporated into the homogenous glass phase prior to partition into crystalline phases at higher concentrations.

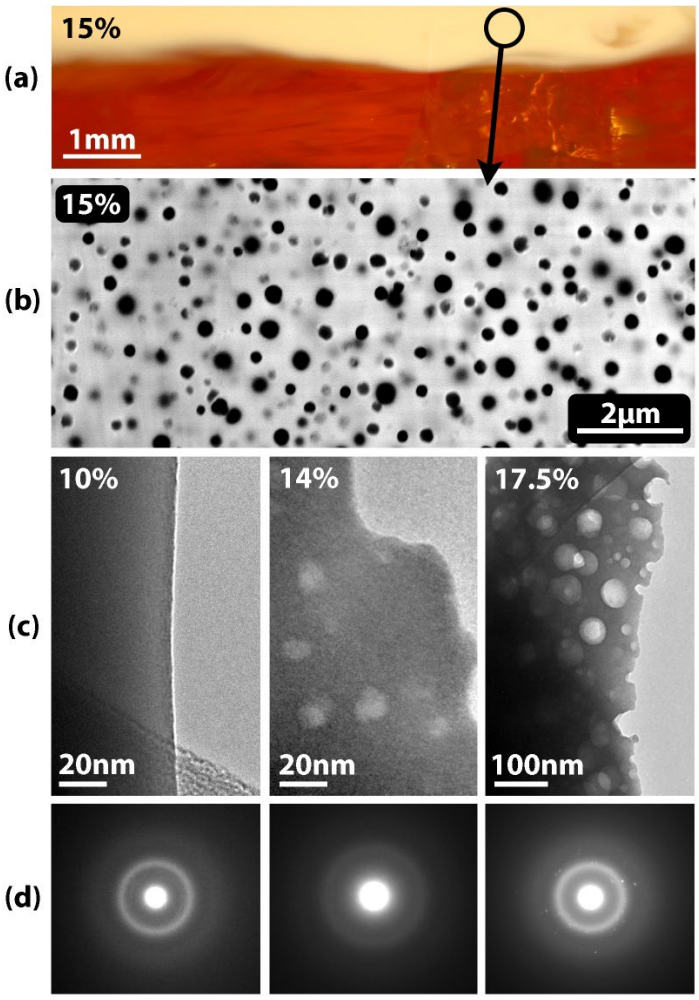

Figure 2-5. (a) Optical micrograph of 15 mass% ER salt 78%TeO_2-22%PbO glass (mass basis). (b) SEM micrograph of the same glass taken from the milky yellow-white phase-separated region on the top of the glass shown in (a). (c) Transmission electron micrograph (TEM) of 78%TeO_2-22%PbO glasses with added 10, 14, and 17.5 mass% ER salt. (d) Selected area diffraction patterns of samples shown in (c). These images are from McCloy et al. (2013) and Riley et al. (2017a).

The compatibility of the 22PbO-78TeO_2 glass was also test for different types of salts simulant regarding loading capacity, thermal property, and chemical durability (Riley et al. 2017a). Three types of chloride salts including $SrCl_2$, oxide reduction (OR) waste salt surrogates for LiCl-Li_2O, and a LiCl-KCl eutectic waste salt called the ER(SF) salt (electrorefiner salt from Steve Frank at Idaho National Laboratory; see Figure 2-6). The prepared salt was mixed and melted with the 22PbO-78TeO_2 glass at different loading fractions. Glasses loaded with $SrCl_2$ showed no crystallization up to 30 mass % loading but a color change was observed at ≥25 mass% loading. For glasses made with the OR salt, phase separation was observed at ≥25 mass% but glasses at ≥18 mass% were increasingly hygroscopic in ambient conditions. Phase separation was observed for glasses made with the ER(SF) salt at waste loadings ≥ 13.5 mass%. Regarding the glass transition temperature, the addition of $SrCl_2$ resulted in an increase while the addition of OR and ER(SF) salts resulted in decreases. Chemical durability was tested with ASTM C1285 tests (powder form in static solution) on the OR salt glasses and ASTM C1308 tests (monolith form in replenished solution) on the ER(SF) glasses. For the release of Te and Pb, results from the C1285

tests tend to show incongruent leaching while the C1308 tests showed congruent leaching due to the inherently different experiment setup. The significant difference in the normalized leaching among elements from both tests suggested the salted loaded glass were phased separated even before the microscopic observation at a lower loading fraction. Compared to mineral waste form options (sodalite and quadridavyne), the 22PbO-78TeO_2 glass offers the benefits of compositional flexibility and a one-step melting process for waste form production. Further investigation is needed to improve the homogeneity of the salt loaded glass for better chemical durability and reduce the amount of TeO_2 used in glass fabrication to lower the cost.

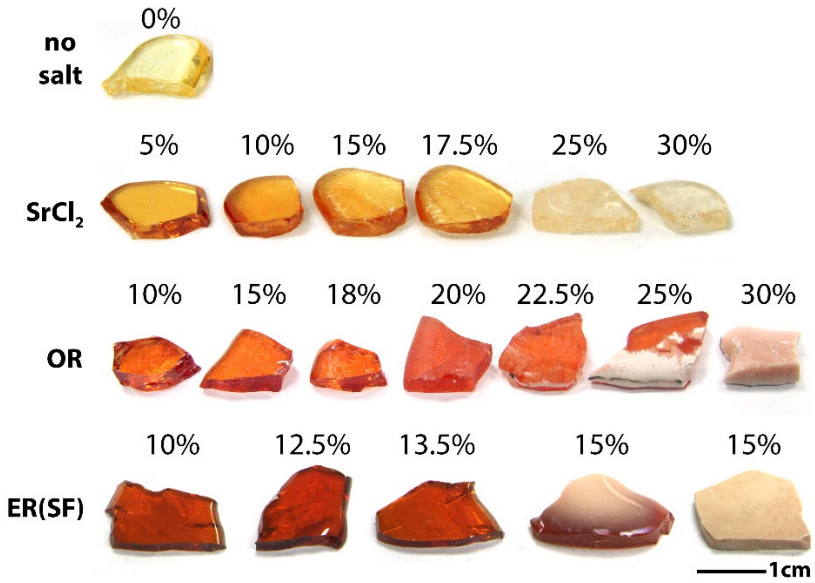

Figure 2-6. Pictures of 78%TeO_2-22%PbO glasses without salt (0%, top) and with varying amounts of $SrCl_2$, OR, and ER(SF) salt loadings. All percentages shown are added salt concentrations to the binary glass listed in mass%. This figure comes from Riley et al. (2017a).

2.1.3 Bismuth Tellurite Glass

Bi_2O_3 was commonly used as an additive in various ternary and quaternary tellurite glass systems to improve the glass formation. However, the binary Bi_2O_3-TeO_2 system has strong crystallization tendency under regular melt-quenching method, and the vitreous state can only be achieved in a narrow composition window using special quenching technique (e.g., ice quench). The glass forming region in the TeO_2-Bi_2O_3-BaO system was studied, and the binary TeO_2–Bi_2O_3 can be vitrified with 5–17 mol% of Bi_2O_3 by quenching the melt between two brass plates (Xu et al. 2011). Zhao et al. examined the Bi_2O_3-B_2O_3-TeO_2 for glass formation under conventional melt-quench method and clear glass was only prepared with Bi_2O_3 < 8 mol% in binary Bi_2O_3-TeO_2 (Zhao et al. 2013). It was claimed the incorporation of Al_2O_3 during the melting with alumina crucible may prompt the glass formation (Zhao et al. 2013). Udovic et al. studied the Bi_2O_3-TiO_2-TeO_2 system and concluded that no glass forming domain can be practically determined within the Bi_2O_3-TeO_2 system except for 0–4 mol% Bi_2O_3 under ice quenching method (Udovic et al. 2006). Similarly, N. Gupta and A. Khanna investigated the $x$$Bi_2O_3$-(100-$x$)$TeO_2$ system with (x = 2, 3, 4, 5, 10 and 20 mol%) and glass was prepared using ice-water quenching with Bi_2O_3 < 5 mol%. The major crystalline phase in samples with Bi_2O_3 ≥ 5 mol% is $Bi_2Te_4O_{11}$ by powder XRD (Gupta and Khanna 2018). Zamyatin et al. systematically studied the ternary system TeO_2-MoO_3-Bi_2O_3 for glass formation and described the Bi_2O_3-TeO_2 system with a small tendency to vitrification with 15–30%

$BiO_{1.5}$ using steel mold quenching method (Zamyatin et al. 2016). The authors claimed the addition of Bi_2O_3 into TeO_2-MoO_3 system has substantially increased the glass forming region (shown in Figure 2-7). The composition with best glass forming ability is $76TeO_2$-$19MoO_3$-$5BiO_{1.5}$ (or $77.9TeO_2$-$19.5MoO_3$-$2.6Bi_2O_3$) with ΔT of 115°C.

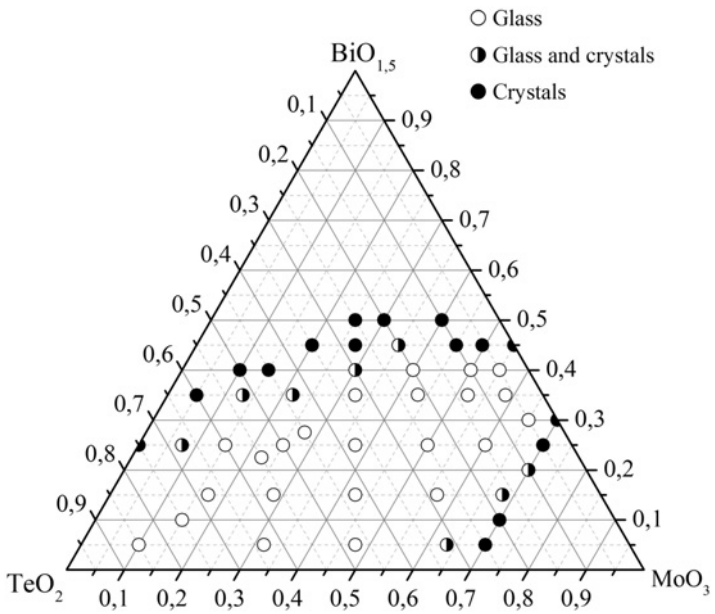

Figure 2-7. Ternary diagram of the TeO_2-MoO_3-Bi_2O_3 system (Zamyatin et al. 2016). The glass-formation region is denoted by boundary encompassed by the open circles.

Ternary Bi_2O_3-$PbCl_2$-TeO_2 glasses were prepared by a melt-quenching method (Ersundua et al. 2021). Batches of these mixtures were melted in closed quartz crucibles at 800°C for 4 min followed by quenching the melt into stainless steel molds. In the Bi_2O_3-$PbCl_2$-TeO_2 system, the vitreous region is strongly confined within the TeO_2-rich side as shown in Figure 2-8. No binary compositions of $PbCl_2$-TeO_2 or Bi_2O_3-TeO_2 were prepared in this study and 9 of 13 ternary compositions were tested amorphous by XRD. Characterization on the thermal properties shown that the glass transition temperature (T_g) increases with increasing Bi_2O_3 or decreasing $PbCl_2$ content at constant TeO_2 content (70 mol%). Glass stability values ($\Delta T = T_c – T_g$) are found to vary between 32 and 110°C and generally decrease with increasing Bi_2O_3 content. The highest glass stability value of 110°C are found with $10Bi_2O_3$-$20PbCl_2$-$70TeO_2$ glass. Increasing Bi_2O_3 or decreasing $PbCl_2$ content for constant TeO_2 do not cause any significant change in molar volume of glasses, whereas the glass network becomes less densely packing by the equimolar substitution of TeO_2 by $PbCl_2$ + Bi_2O_3 and increasing Bi_2O_3 content indicated by the increased oxygen molar volume and decreased oxygen packing density. The average cross-link density also decreased with increasing Bi_2O_3 content in glass.

Ternary glasses with compositions of $(100\text{-}y)TeO_2$-$yPbO$-$10Bi_2O_3$ where y = 0, 5, 10, 15, 20, and 25 mol% were prepared using a conventional melt-quenching method (Ahmed and Mawlud 2023). The batches were melted in an alumina crucible at 1000°C for 25 minutes prior to quenching. X-ray diffraction (XRD) confirmed the amorphous nature of all prepared samples including the binary one of $90TeO_2$-$10Bi_2O_3$. Molar volume, oxygen packing density, and optical basicity decreased with PbO substituting for TeO_2 in the glasses.

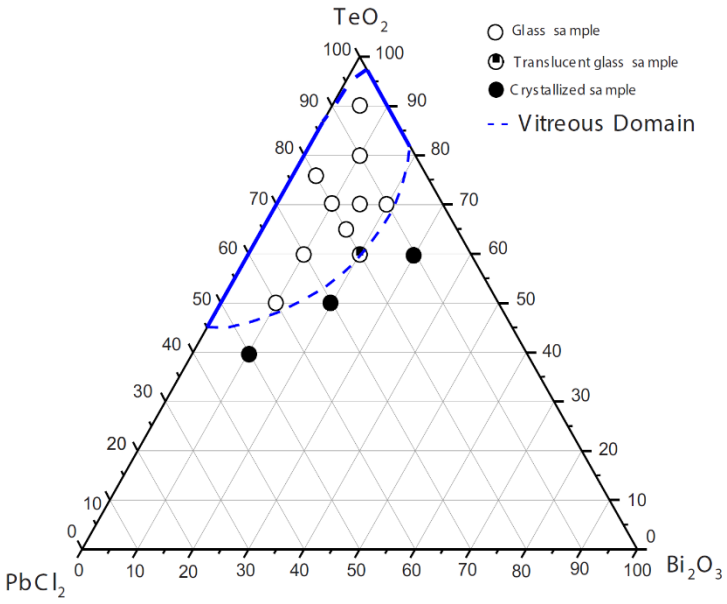

Figure 2-8. Ternary diagram of the Bi_2O_3-$PbCl_2$-TeO_2 system (Ersundua et al. 2021). The glass-forming region is denoted in blue.

2.1.4 Other Tellurite Glass

Binary xB_2O_3-(100-x)TeO_2 with x = 15, 20, 25, 30 and 35 mol% and ternary glasses: yAl_2O_3-$10B_2O_3$-(100-y)TeO_2: y = 5, 10, 20, 30 mol% were prepared using H_3BO_3, α-Al_2O_3 and TeO_2 (Kaur and Khanna 2014). The mixture was sintered at 250°C for 24 h and melted at 800°C for about 30 minutes in platinum crucible. For binary borotellurite system, clear transparent glasses were made up to 30 mol% of B_2O_3. Aluminoborotellurite glasses required higher quenching rates by splat quenching for the formation of glassy phase. An amorphous–amorphous phase separation was observed at an alumina concentration of ≥ 10 mol%. Adding Al_2O_3 into the B_2O_3-TeO_2 system improves the chemical durability to atmospheric water vapor, but the homogeneous glass (T_g ≈ 346°C) can only be formed at low Al_2O_3 concentration of 5 mol%.

In a study by Dwaikat et al. (2021), 20BaO-10SrO-30TeO_2-(40-x)B_2O_3-$xMoO_3$ glasses (x = 0, 5, 10, and 15) were prepared by melting the batched mixture at 1000°C for 20 minutes. The melt was quenched by pouring onto a steel plate. Density of the glass increased with MoO_3 replacing the B_2O_3. Weight loss measurement shown that the glass with 10 mol% MoO_3 has the best chemical durability (1.712×10^{-4} g/cm^2/d in a 28-day test at room temperature) amongst all candidates tested.

A study was performed in 2010 by Riley and Rieck (2010) where a variety of tellurite glass systems were evaluated for immobilizing and incorporating a salt waste simulant. In that study, a TeO_2-PbO-Bi_2O_3 glass was produced (T2G-12). This sample showed a mostly glassy matrix with some crystalline inclusions (see Figure 2-9).

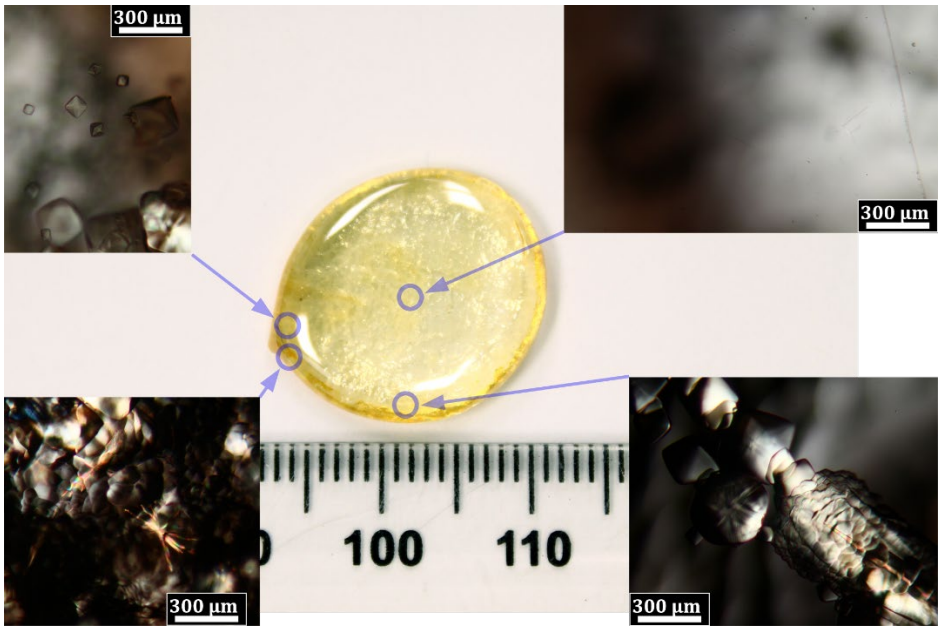

Figure 2-9. Pictures of 77.6%TeO_2–19.3%PbO–3.1%Bi_2O_3 glass (T2G-12, mass basis) from a 2010 study at PNNL (pictures courtesy of Bennett Rieck, unpublished).

2.2 Zinc Bismuth Glass

Low-temperature sintering was evaluated for ZnO-Bi_2O_3-SiO_2 to maximize retention of ^{129}I by forming the mixture of AgI salt (25 mass% loading) or AgI-mordenite (20 mass% loading with 5 mass% silver) with glass powder into a dense composite material (Garino et al. 2011). This was achieved through a low-temperature sintering method by uniaxially pressing the dry mixtures at 70 MPa in a steel die followed by the heating in air to 550°C in 1 hour. In the thermogravimetric analyses (TGA), no obvious mass loss with observed for the Zn-Bi-Si-glass (75 mass%)/AgI (25 mass%) sample, and the Zn-Bi-Si-glass (glass/AgI–mordenite/Ag mixture by 80:20:5, by mass, respectively) sample showed a loss of 8.3 mass%. The short-term chemical durability was studied in a modified PCT-B test and results indicated both composite waste forms had chemical durability like Pyrex glass with extremely low levels of iodine release into solution.

The base glass systems of ZnO-Bi_2O_3-B_2O_3 and ZnO-Bi_2O_3-SiO_2 was first examined on their thermal properties and crystallization behavior to select the candidate binder material for low temperature sintering (Lere-Adams et al. 2022). In general, the silicate glasses required higher melting temperatures and longer melting times than the borate glasses. Among all glasses tested, the 25ZnO-15Bi_2O_3-60B_2O_3 glass exhibited the best performance of the largest sintering window (186°C) with $T_g \approx 513$°C. Several glasses were further studied for the immobilization of radioiodine from caustic scrubber wastes in comparison with other candidate materials (Lere-Adams et al. 2024). Glass binders were mixed with waste simulants (sodalite-rich material), uniaxially pressed into pellets, and sintered at 350°C or 550°C for 8 hours in air. Iodine retention was 67–100% in the final waste forms. The 25ZnO-15Bi_2O_3-60B_2O_3 glass waste form showed the best aqueous durability in terms of the lowest cumulative iodine release. The matrix of samples tested by Lere-Adams et al. (2024) is presented in Table 2-2 and the ZnO-Bi_2O_3-B_2O_3 ternary phase diagram of that study is presented in Figure 2-10.

Table 2-2. Compositions in the silicate and borate systems. Listed also are melting conditions, XRD-observed phase after quenching (AQ) if any, glass transition temperature (T_g) and sintering window ($\Delta T = T_{x,\,onset} - T_g$) (Lere-Adams et al. 2022)

#	ZnO (mol%)	Bi_2O_3 (mol%)	SiO_2 (mol%)	B_2O_3 (mol%)	Synthesis Conditions	Phases Observed AQ by XRD	T_g (°C)	ΔT (°C)	Down-Selected
1	25	50	25	-	1400°C-1 hour	Glass	376	62	X
2	60	15	25	-	1400°C-1 hour	Zn_2SiO_4, ZnO, $Bi_{12}SiO_{20}$	578	40	
3	25	15	60	-	1100°C-2 hour	No melt	-	-	
4	20	40	40	-	1000°C-1 hour	Glass	405	39	
5	20	30	50	-	1000°C-1.5 hour	Glass	500	33	
6	30	20	50	-	1000°C-1.5 hour + 1100°C-2 hour	Glass	533	43	
7	50	20	30		1400°C-1 hour	$Bi_{12}SiO_{20}$	488	71	X
8	25	50	-	25	1000°C-1 hour	Glass	363	24	X
9	60	15	-	25	1000°C-1 hour	$Zn_3B_2O_6$, $Bi_4B_2O_9$	447	36	
10	25	15	-	60	1000°C-1 hour	Glass	513	186	X

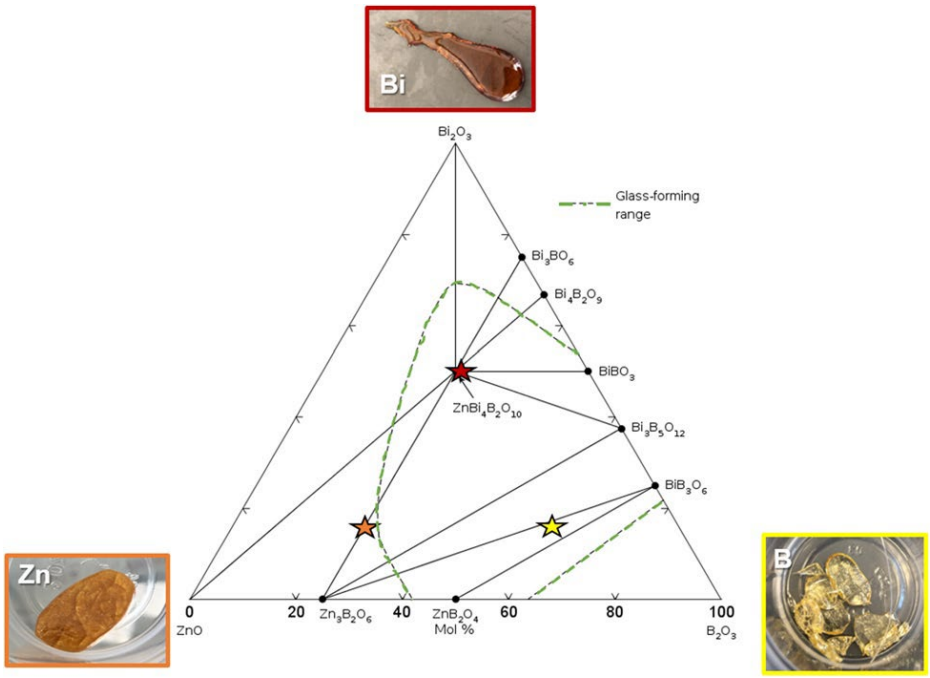

Figure 2-10. Ternary phase diagram of ZnO-Bi_2O_3-B_2O_3 system showing compositional location of studied samples in or near the borate glass forming region. Insert photo borders have colors matched to symbols, and the numbers shown correspond to Table 2-2 (Lere-Adams et al. 2022).

2.3 Phosphate Glass

Phosphate glasses have been explored under the Material Recovery and Waste Form Development (MRWFD) Campaign since 2017. This work has resulted in several publications between Pacific Northwest National Laboratory and Argonne National Laboratory (Ebert et al. 2018; Riley and Chong 2020; Riley et al. 2020; Riley and Chong 2021; Riley et al. 2021; Riley et al. 2023a; Riley et al. 2023b; Riley et al. 2023c; Marcial et al. 2024; Murray et al. 2024). This work was initiated based on work done prior to that with reactions between phosphate compounds (i.e., $NH_4H_2PO_4$ and H_3PO_4) (Donze et al. 2000; Donze et al. 2001; Siemer 2012) and different halide

salt mixtures combined with knowledge learned in related studies from the late 1990s to the 2020s with chemically durable iron phosphate glasses (Day et al. 1998; Mesko et al. 2000; Kim and Day 2003; Kim et al. 2003; Day and Ray 2013; Ma et al. 2017; Brow et al. 2020; Bai et al. 2021). An example of the variability in chemical durability with changing oxygen-to-phosphorus ratios in phosphate glasses is provided in Figure 2-11, which spans several orders of magnitude. From these past studies, it was determined that the $40Fe_2O_3$-$60P_2O_5$ (mol%) binary glass was the most promising formulation for this binary system in terms of chemical durability.

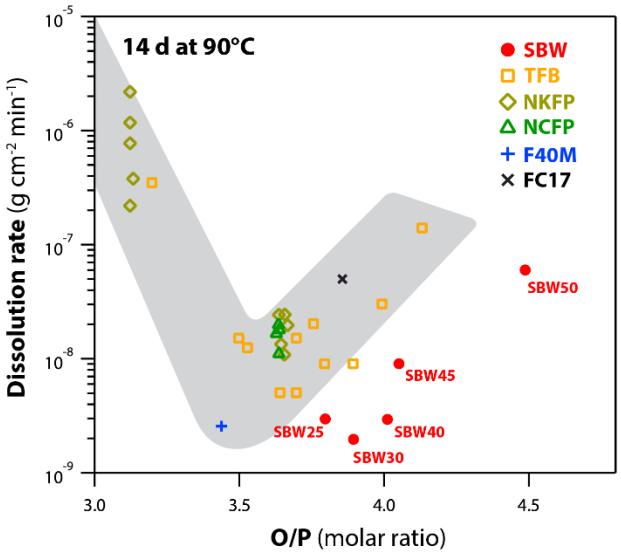

Figure 2-11. Compiled dissolution rates for phosphate glasses mixed with various simulated waste compositions as a function of [O]/[P] ratio. This figure was modified from the original by Day and Ray (Day and Ray 2013) and Marcial et al. (2024).

The compatibility of the $40Fe_2O_3$-$60P_2O_5$ binary glass to incorporate CsCl and SrF_2 was studied (Mesko et al. 2000). In these samples, CsCl was added up to 26.2 mol% solely and up to 12.4 mol% along with SrF_2 (21.9 mol%). Batches were prepared with Fe_2O_3, P_2O_5, CsCl, and SrF_2, and they were melted in alumina crucible between 950–1200°C for 1–2 hours. The heat-treatment was initialized from 800°C and the melt was stirred twice. Lower melting temperature is needed for high halide glass due to the decrease of melt viscosity. The retention of chlorine is very low (<9.8 atomic%) in the final glass likely due to the volatilization during melting. The leaching of phosphorus in 7-day PCT test at 90°C (ASTM C1285-94; ASTM is the American Society for Testing and Materials International) is ranging between 1.5–2.9 mg/L. The overall dissolution rate is inversely proportional to the number of Fe–O–P bonds in glass.

The behavior of potassium iron phosphate glass was investigated with the addition of $FeCl_3$ (Moustafa 1999). Nominal glasses $10Fe_2O_3$-$55P_2O_5$-$x FeCl_3$-$(35-x)K_2O$ were batched with Fe_2O_3, $NH_4H_2PO_4$, $FeCl_3$, and K_2CO_3. $NH_4H_2PO_4$ was preheated at 300°C for 1 hour and other batch chemicals were added then heat-treated at 600°C for 30 minutes. The batch was melted in a covered porcelain crucible between 1000-1200°C for 30 minutes and the crucible was periodically swirled during melting for homogeneity. The retention of chloride in the fabricated glass was claimed to be > 99 mass%. The dissolution rate measured in HCl solution (1.6 M) @60°C is 10^{-10} to $10^{-10.625}$ mg/(cm^2·h), which is better than window glass.

Spent electrolyte salts (25.7% LiCl, 31.6% KCl, 4.1% CsCl, 5.1% $BaCl_2$, 3.8% $SrCl_2$, 29.7% $LaCl_3$, in mass%) was incorporated into $40Na_2O$-$10Al_2O_3$-$10Fe_2O_3$-$40P_2O_5$ glass with 10 mass% salt

loading (Kulikova et al. 2021). The batch was melted in quartz crucible at 1200°C for 1 hour and the quenched sample was confirmed as X-ray amorphous. The chlorine retention was estimated to be around 35 mass% using XRF and SEM-EDS. The release rate of sodium in semi-dynamic dissolution test at 90°C was less than 3×10^{-6} g/(cm^2 day). Additionally, an iron phosphate glass composite materials was fabricated to host the same spent electrolyte salts (Frolova et al. 2023). The pressed pellet was prepared under 5 MPa and sintered at 700°C for 4 hours with precursor glass powder ($40Fe_2O_3$-$60P_2O_5$) and the mixed dry salt 25.7% LiCl, 31.6% KCl, 4.1% CsCl, 5.1% $BaCl_2$, 3.8% $SrCl_2$, 29.7% $LaCl_3$, in mass%). The retention of chlorine in the final sample was estimated to be around 70 mass%. Major crystalline phases in the composite were $FePO_4$, $KFe(P_2O_7)$, $LiFe(P_2O_7)$, and $Fe_4(P_2O_7)_3$. Elemental leaching was tested using PCT method (ASTM C1285) and the results were P = 8.4×10^{-7} g/(cm^2 day), Fe = 1.3×10^{-10} g/(cm^2 day), La = 1.8×10^{-8} g/(cm^2 day), Sr = 4.1×10^{-6} g/(cm^2 day), and Cs = 1.2×10^{-6} g/(cm^2 day). These values are comparable to those from the iron phosphate glasses.

2.4 Recommendations for Experiments

This section provides the recommendations for testing in the current study based on the review of available literature.

2.4.1 Fe_2O_3-P_2O_5 Glass System

Due to extensive research on the Fe_2O_3-P_2O_5 binary system (namely the $40Fe_2O_3$-$60P_2O_5$ composition, by mole) (Kim et al. 2003; Hsu et al. 2013; Hsu et al. 2014; Riley et al. 2020), this system was explored. The addition of halide salt lowers the melting temperature (<1000°C) of $40Fe_2O_3$-$60P_2O_5$ glass which can potentially reduce the volatilization of the salt components during melting. Other studies on various alkali Fe_2O_3-P_2O_5 glasses and glass-ceramics demonstrate the good chemical durability with the high retention of chloride salts. Due to the abilities of salt/acid-based phosphate reagents used to create phosphate glass to remove halogens during high-temperature processing (Riley et al. 2020; Murray et al. 2024; Werth et al. 2025), the approach recommended for this glass system is to add salt to pre-made glass frit followed by a heat treatment.

2.4.2 MoO_3-Bi_2O_3-TeO_2 Glass System

The ternary MoO_3-Bi_2O_3-TeO_2 glass presents a large glass-forming region using the regular melt-quench method for glass fabrication. The glass compositions and melting conditions of several ternary and quaternary systems are summarized in Table 2-3. After comparing the MoO_3-Bi_2O_3-TeO_2 systems reported in literature, it appears the $20MoO_3$-xBi_2O_3-$(80-x)TeO_2$ (x = 2.5, 5, and 10 mol%) has reasonably good glass-forming ability to be prepared under the conventional melt-quench method. The proposed melting conditions can be 800°C for 30 minutes in platinum crucibles with 20-gram batches.

Table 2-3. MoO_3-Bi_2O_3-TeO_2 glass systems reported in literature.

Glass System (mol%)	Crucible	Heat Treatment	Batch Size	Reference
MoO_3-Bi_2O_3-TeO_2 ($19.5MoO_3$-$2.6Bi_2O_3$-$77.9TeO_2$ with best forming ability)	Porcelain	850°C for 15 minutes	5 grams	Zamyatin et al. (2016)
$20MoO_3$-$10Bi_2O_3$-$70TeO_2$-$1Er_2O_3$	Platinum	750°C for 2 hours	N/A	Li and Man (2009)
$75TeO_2$-$10MoO_3$-10BaO-$5Bi_2O_3$	Platinum	800°C for 1 hour	N/A	Alzahrani et al. (2023)
$20MoO_3$-xBi_2O_3-(80-x)TeO_2 x = 10, 15, 20, 25 mol%	N/A	N/A	N/A	Itas et al. (2024)

2.4.3 PbO-Bi_2O_3-TeO_2 Glass System

Previous work on the binary PbO-TeO_2 glass showed its good chemical durability with relatively high salt loading. However, the glass-forming region is narrow in the binary PbO-TeO_2 glass system, and it is primarily restricted to the 22PbO-$78TeO_2$ ($16.8PbO$-$83.2TeO_2$ in mol%) composition. Also, Bi_2O_3 has been used as an additive component in binary tellurite glasses to improve the glass-forming ability. It could be beneficial to add Bi_2O_3 into the PbO-TeO_2 system to extend the glass forming region to the side with lower TeO_2 fraction. Two ways of adding Bi_2O_3 for the preparation of two glass series: (a) xBi_2O_3-(100-x)($0.168PbO$-$0.832TeO_2$) (x = 5, 10, 15) and (b) $10Bi_2O_3$-yPbO-(90-y)TeO_2 (y = 15.12, 25, 35). The overlapping composition between the two different glass series is $10Bi_2O_3$-$15.12PbO$-$74.88TeO_2$.

2.4.4 Ag_2O-WO_3-TeO_2 Glass System

The Ag_2O-WO_3-TeO_2 glasses show reasonably good performance for the retention of AgI without sacrificing much of the chemical durability. Glass fabrication requires relatively low melting temperature (< 850°C) and short melting time (< 1 hour), which could contribute to the high retention of halide salts with reduced volatilization. It would be useful to assess the compatibility of the Ag_2O-WO_3-TeO_2 glass to process with chloride salts. The glass composition of $30Ag_2O$-$35WO_3$-$35TeO_2$ may be considered for experimental investigation on the incorporation of chloride salts and the corresponding effect on chemical durability.

2.4.5 ZnO-Bi_2O_3-(B_2O_3/SiO_2) Glass System

Several glass compositions in Table 2-2 showed feasible synthesis conditions with relatively low melting temperature of 1000°C and short melting times of 1 hour. These conditions are likely to help with reducing the volatility of salt during heat-treatment processing. Among these glasses, $25ZnO$-$15Bi_2O_3$-$60B_2O_3$/SiO_2 showed the best glass stability (ΔT = 186°C) and no crystals were formed in the quenched glass. Compositions of $20ZnO$-$40Bi_2O_3$-$40SiO_2$ and $25ZnO$-$50Bi_2O_3$-$25B_2O_3$ produced amorphous samples after quenching, which suggests reasonably good glass forming ability. All three glass compositions were recommended for testing with the mixture of chloride salt using the synthesis conditions of 1000°C for 1 hour.

3.0 Experimental Work

3.1 ERV3 Salt Preparation

This section describes the processes used for producing the ERV3 salt simulant, the composition of which is shown in Table 3-1. Reagent salts were purchased at 99.5% or better purity, as seen in Table 3-2. Salts were handled inside an argon atmosphere glovebox maintained at < 10 ppm oxygen (O_2) and < 1 ppm moisture (H_2O). A straight-wall Inconel crucible and an Inconel lid purchased from Sigma Aldrich were cleaned using a wire brush and wiped with methanol. Mixtures of reagents were batched directly into the crucible by mass per Table 3-1 using a Mettler Toledo analytical balance (± 0.01 g). The salt was then mechanically mixed inside the crucible and heated in a well furnace to 200°C for 18 hours to drive off adsorbed water and then heated to 500°C for 8 hrs to fuse the salt. The mixture was removed from the crucible and broken up into pieces of < 1 cm^3. The mixture appeared heterogeneous, so it was reloaded into the crucible and heated at 600°C for an additional 8 hrs. After cooling, the salt was removed from the crucible and crushed using a hammer and chisel into pieces < 1 cm^3 in size. All salt facing implements were cleaned with methanol prior to use. The salt appeared homogeneous after the second fusing and was packaged into a clean glass jar. The jar was removed from the glovebox, sealed in a vacuum bag for transport, and then shipped to PNNL.

Table 3-1. Target composition of the ERV3 salt in mass fractions.

Component	Mass%
KCl	0.390578
LiCl	0.320474
NaCl	0.090133
$CeCl_3$	0.050074
$NdCl_3$	0.048672
$SrCl_2$	0.029964
CsCl	0.070104
Total	1.000000

Table 3-2. Batched Composition of ERV3 salt for use at Argonne National Laboratory. TSC denotes Thermo Scientific Chemicals.

Salt	Supplier/Purity	Mass (g)	Mass%
LiCl	Apollo Scientific/ Anhydrous 99.9%	80.01	32.00
KCl	Millipore Sigma/ ≥99.5%	97.50	39.00
NaCl	TSC/ Ultra Dry 99.99% metals basis	22.50	9.00
$CeCl_3$	TSC / Ultra Dry ≥99.9% REO basis	12.52	5.00
$NdCl_3$	TSC/ Anhydrous ≥99.9% REO basis	12.50	5.00
$SrCl_2$	TSC/ Anhydrous 99.99% trace metals basis	7.51	3.00
CsCl	TSC / Ultra Dry ≥99.9% metals basis	17.50	7.00

3.2 Glass Fabrication

Glasses were fabricated in different phases with details provided in Table 3-3. Seven different sets (i.e., **A**–**G**) were prepared starting with a melt-quench of frits (without any salt simulant) and the frits were then mixed with salt simulant and prepared through subsequent heat treatments. The general composition in each set is consistent but the samples vary between salt (ERV3) loadings (see Table 3-1) and heat-treatment processes. The samples prepared by the two heat-treatment methods will be referred as "fast cooled" by melt-quench, and "slow cooled" by furnace cool in the rest of this report. Additional details for ERV3 synthesis are provided in Section 3.1.

Table 3-3. Summary of glass and salt-loaded glass prepared broken out by set, sample ID, glass composition, salt loading, and heat-treatment method.

Set	Sample ID	Nominal Glass Composition (mol%)	ERV3 Salt Loading (mass%)	Heat-Treatment Method
A	Fe-P	$40Fe_2O_3$-$60P_2O_5$	0	Melt-quench
	Fe-P-0ERV3-F	$40Fe_2O_3$-$60P_2O_5$	0	Furnace cool
	Fe-P-10ERV3-F	$40Fe_2O_3$-$60P_2O_5$	10	Furnace cool
	Fe-P-20ERV3-F	$40Fe_2O_3$-$60P_2O_5$	20	Furnace cool
B	Zn-Bi-Si	$20ZnO$-$40Bi_2O_3$-$40SiO_2$	0	Melt-quench
	Zn-Bi-Si-10ERV3-Q	$20ZnO$-$40Bi_2O_3$-$40SiO_2$	10	Melt-quench
	Zn-Bi-Si-10ERV3-F	$20ZnO$-$40Bi_2O_3$-$40SiO_2$	10	Furnace cool
C	Zn-Bi-B-1	$25ZnO$-$15Bi_2O_3$-$60B_2O_3$	0	Melt-quench
	Zn-Bi-B-1-10ERV3-Q	$25ZnO$-$15Bi_2O_3$-$60B_2O_3$	10	Melt-quench
	Zn-Bi-B-1-10ERV3-F	$25ZnO$-$15Bi_2O_3$-$60B_2O_3$	10	Furnace cool
D	Zn-Bi-B-2	$25ZnO$-$50Bi_2O_3$-$25B_2O_3$	0	Melt-quench
	Zn-Bi-B-2-10ERV3-Q	$25ZnO$-$50Bi_2O_3$-$25B_2O_3$	10	Melt-quench
	Zn-Bi-B-2-10ERV3-F	$25ZnO$-$50Bi_2O_3$-$25B_2O_3$	10	Furnace cool
E	Mo-Bi-Te-1	$20MoO_3$-$2.5Bi_2O_3$-$77.5TeO_2$	0	Melt-quench
	Mo-Bi-Te-1-10ERV3-Q	$20MoO_3$-$2.5Bi_2O_3$-$77.5TeO_2$	10	Melt-quench
	Mo-Bi-Te-1-10ERV3-F	$20MoO_3$-$2.5Bi_2O_3$-$77.5TeO_2$	10	Furnace cool
F	Mo-Bi-Te-2	$20MoO_3$-$5Bi_2O_3$-$75TeO_2$	0	Melt-quench
	Mo-Bi-Te-2-10ERV3-Q	$20MoO_3$-$5Bi_2O_3$-$75TeO_2$	10	Melt-quench
	Mo-Bi-Te-2-10ERV3-F	$20MoO_3$-$5Bi_2O_3$-$75TeO_2$	10	Furnace cool
G	Mo-Bi-Te-3	$20MoO_3$-$10Bi_2O_3$-$70TeO_2$	0	Melt-quench
	Mo-Bi-Te-3-10ERV3-Q	$20MoO_3$-$10Bi_2O_3$-$70TeO_2$	10	Melt-quench
	Mo-Bi-Te-3-10ERV3-F	$20MoO_3$-$10Bi_2O_3$-$70TeO_2$	10	Furnace cool

3.2.1 Fe_2O_3-P_2O_5 Glass

The $40Fe_2O_3$-$60P_2O_5$ (molar basis) binary glass was fabricated using conventional melt-quench method. Raw chemicals of ammonium dihydrogen phosphate (ADP, or $NH_4H_2PO_4$) and iron (III) oxide (Fe_2O_3) were weighed and homogenized in an alumina crucible (AdValue, 250mL, AL-1250), placed into furnace at room temperature (Deltech®), with 5°C/min heating to 400°C. At this temperature, a 1-hour hold time was performed to decompose ADP and mitigate potential late-stage glass-melt foaming. After the delay, the 5°C/min heating continued to 1150°C with a final

hold for 1-hour for homogenization, followed by a quench on an Inconel pour plate. The quenched glasses were milled and sieved into fine powder (< 75 µm) for further experiments.

3.2.2 ZnO-Bi_2O_3-B_2O_3/SiO_2 Glass

Three binder glasses were selected based on the melting condition and thermal properties reported in Table 2-2. The nominal compositions of the glasses are $20ZnO$-$40Bi_2O_3$-$40SiO_2$, $25ZnO$-$15Bi_2O_3$-$60B_2O_3$, and $25ZnO$-$50Bi_2O_3$-$25B_2O_3$. 40-gram batches were prepared using reagent grade chemicals of oxides, followed by a hand-mixing step for 5 min. The mixed batches were melted using a covered Pt/Au crucible at 1000°C for 1 hour. The volatilization and viscosity of the melt was observed prior to quenching onto a stainless-steel plate. The quenched glasses were characterized by XRD to check for any crystal formation. Glasses were milled and sieved into fine powder (<75 µm) for further experiments.

3.2.3 MoO_3-Bi_2O_3-TeO_2 Glass

Glasses with nominal composition of $20MoO_3$-xBi_2O_3-$(80-x)TeO_2$ (x = 2.5, 5, and 10 mol%) were fabricated using regular melt-quench method. Reagent-grade oxides were weighed and mixed for a 20-gram batch prior to melting in a covered Pt/Au crucible. The melt was held at 800°C for 30 minutes and then quenched onto a stainless-steel plate. The volatilization and viscosity of the melt was determined visually. The quenched glasses were characterized by XRD to check for any crystal formation. Glasses were milled and sieved into fine powder (< 75 µm) for further experiments.

3.3 Preparation of Salt-Loaded Glasses

3.3.1 Fast Cooling by Melt-Quench Process

ERV3 salt was mixed with the glass powder (< 75 µm) and processed with the regular melt-quench method. For each sample, the mixture (≈ 5 gram) was melted in a covered Pt/Au crucible under the same condition used to fabricate the base glass, followed by quenching the melt onto an Inconel plate. XRD and SEM-EDS were applied to analyze the structure and chemistry of the samples.

3.3.2 Slow Cooling by Heat-Treatment

For the $40Fe_2O_3$-$60P_2O_5$ binary glass, the ERV3 salt was mixed with the glass powders at different salt loading (0, 10 and 20 mass%). Samples were heat-treated in a covered alumina crucible using a muffle furnace. The furnace was set to ramp from room temperature to the desired melting temperature at 5°C/minute. The sample was held at the melting temperature for specific time prior to furnace cooling to room temperature. For ZnO-Bi_2O_3-B_2O_3/SiO_2 and MoO_3-Bi_2O_3-TeO_2 glasses, mixture (≈ 2 g) of glass powder (< 75 µm) and ERV3 salt was loaded into a Pt/Au boat (1.2 cm × 1.2 cm square bottom). The Pt boat was closed with a lid to minimize volatilization during the heat-treatment inside a muffle furnace. Similar heating profile was used for heat-treatment as described earlier for the $40Fe_2O_3$-$60P_2O_5$ binary glass. The total weight of the Pt/Au boat with sample was recorded before and after heat-treatment to determine the weight loss.

3.4 Characterization of Samples

3.4.1 Density

The density of each sample was determined using a helium pycnometer. Solid pieces were weighed before volume measurement on an analytical balance (±0.1 mg; Mettler Toledo MS204TS/00), and the density was calculated by dividing the sample mass by the volume measured. The density of each sample was reported as an average of 10 measurements along with a standard deviation.

3.4.2 X-Ray Diffraction

The samples were ground into fine powders in a tungsten carbide milling chamber. X-ray diffraction (XRD) analysis was performed with a Bruker D8 Advance (BrukerAXS Inc., Madison, WI) equipped with a Cu Kα target (λ =1.5406 Å) and a LynxEye™ position-sensitive detector at 40 kV and 40 mA. Powders of each sample were mounted in 10 mm holders and scanned from 5−90° (2θ), with a step size of 0.015° (2θ), and a dwell of 0.3 s per step. Bruker AXS DIFFRAC^{plus} EVA was used to identify the crystalline phases present in the samples.

3.4.3 Scanning Electron Microscopy and Energy Dispersive Spectroscopy

Powdered samples were adhered to a sample stub with double-sided carbon tape and then sputter coated with Ir to reduce charging. Scanning electron microscopy (SEM) was conducted on a JEOL JSM 7001F/TTLS LV equipment at 15 kV and 2 nA. Energy dispersive spectroscopy (EDS) data were collected from six regions on each sample to estimate the elemental composition of the samples.

4.0 Results

4.1 Details of Slow-Cooling Heat Treatment

Details on the heat-treatment test of samples are given in Table 4-1. In general, MoO_3-Bi_2O_3-TeO_2 glasses heat-treated at lower temperature (800°C) and short time (0.5 hour) appear to have less weight loss than the ZnO-Bi_2O_3-B_2O_3/SiO_2 glasses heat-treated at 1000°C/1 hour under the same salt loading (10 mass% ERV3).

Table 4-1. Heat-treatment of slow-cooled glass mixed with ERV3 salt in Pt/Au boats.*

Set	Glass System (mol%)	ERV3 Salt Loading (in mass%)	HT Condition [*T*(°C)/*t*(hr)]	Observation of Sample After HT	Mass Loss After HT (mass%)
A	$40Fe_2O_3$-$60P_2O_5$	0	1000/1	Amorphous	-0.40%
	$40Fe_2O_3$-$60P_2O_5$	10	1000/1	Crystalized	4.15%
	$40Fe_2O_3$-$60P_2O_5$	20	1000/1	Crystalized	8.70%
B	20ZnO-$40Bi_2O_3$-$40SiO_2$	0	1000/1	Crystallized	-0.11%
	20ZnO-$40Bi_2O_3$-$40SiO_2$	10	1000/1	Crystallized	10.16%
C	25ZnO-$15Bi_2O_3$-$60B_2O_3$	0	1000/1	Clear with no inclusion	1.96%
	25ZnO-$15Bi_2O_3$-$60B_2O_3$	10	1000/1	Clear with no inclusion	9.87%
D	25ZnO-$50Bi_2O_3$-$25B_2O_3$	0	1000/1	Clear with no inclusion	-0.10%
	25ZnO-$50Bi_2O_3$-$25B_2O_3$	10	1000/1	Crystallized and overflown	27.08%
E	$20MoO_3$-$2.5Bi_2O_3$-$77.5TeO_2$	0	800/0.5	Clear with no inclusion	1.25%
	$20MoO_3$-$2.5Bi_2O_3$-$77.5TeO_2$	10	800/0.5	Clear with no inclusion	6.24%
F	$20MoO_3$-$5Bi_2O_3$-$75TeO_2$	0	800/0.5	Clear with no inclusion	1.15%
	$20MoO_3$-$5Bi_2O_3$-$75TeO_2$	10	800/0.5	Clear with no inclusion	6.67%
G	$20MoO_3$-$10Bi_2O_3$-$70TeO_2$	0	800/0.5	Crystalized	1.68%
	$20MoO_3$-$10Bi_2O_3$-$70TeO_2$	10	800/0.5	Opaque	6.69%

*HT denotes heat treatment, *T* denotes HT temperature (in °C), *t* denotes heat treatment time (in hours).

4.2 Visual Appearances

Slow-cooled Fe-P samples are shown in Figure 4-1. The Fe-P samples loaded with 0 mass% and 10 mass% ERV3 appear mostly glassy, while the sample loaded with 20 mass% ERV3 is extensively crystalized. The appearances of the remaining compositions are provided in Figure 4-2. Inclusions are observed in 20ZnO-$40Bi_2O_3$-$40SiO_2$ and $20MoO_3$-$10Bi_2O_3$-$70TeO_2$ appears partially opaque. All other fast-cooled glasses are transparent without inclusions. For the fast-cooled samples, the addition of ERV3 salt leads to the devitrification of the 25ZnO-$50Bi_2O_3$-$25B_2O_3$ glass and surface patterns were also observed for the 20ZnO-$40Bi_2O_3$-$40SiO_2$ glass

suggesting partial crystallization. For the slow-cooled samples loaded with ERV3 salt, 25ZnO-15Bi_2O_3-60B_2O_3, 20MoO_3-2.5Bi_2O_3-77.5TeO_2, and 20MoO_3-5Bi_2O_3-75TeO_2 appear as glassy.

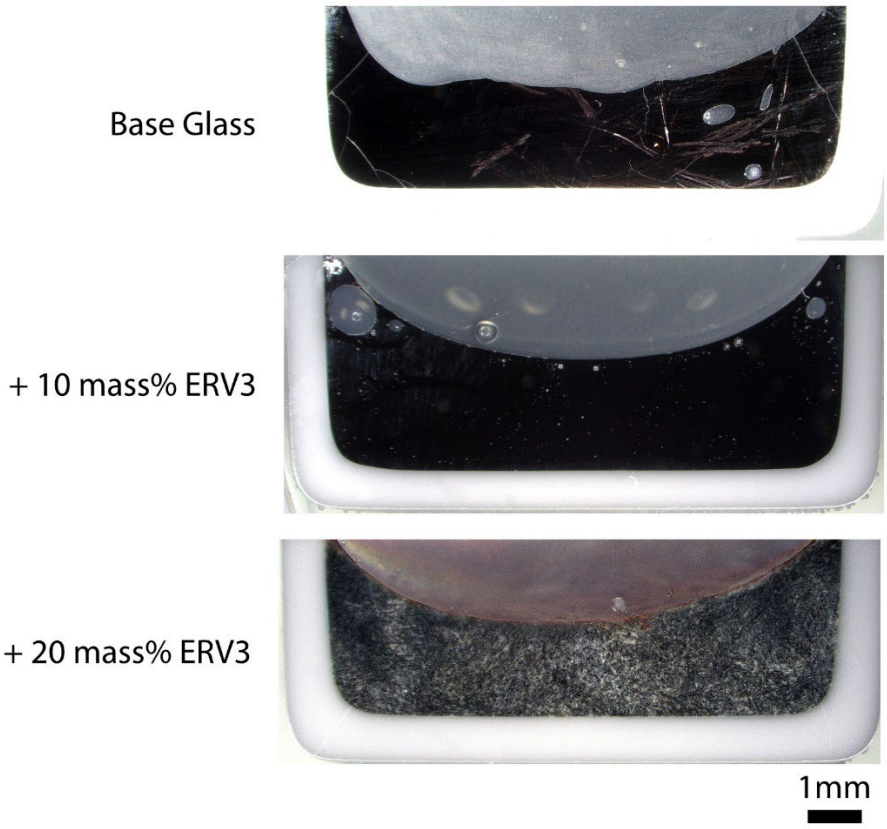

Figure 4-1. Polished cross-sectional images of Fe-P slow-cooled samples (set A), including (top) the base glass, (middle) the sample with 10 mass% ERV3, and (bottom) the sample with 20 mass% ERV3. All samples are shown embedded in their original alumina crucibles.

Figure 4-2. Images of glasses and samples with salt addition. Glass compositions are in mol%.

4.3 Density Data

The bulk density measurements from helium pycnometry (i.e., $\rho_{ave} \pm \rho_{stdev}$) are presented below in Table 4-2. The glasses tested in this study varied notably in ρ_{ave} with some glasses being > 7 g/cm^3 and the Fe-P glass being much lower (≈ 3 g/cm^3). In general, the ERV3 salt decreased the ρ_{ave} value from the base (frit) glass with the fast cooled glasses showing the lowest ρ_{ave} values in each series. Also, the associated errors were low, and fluctuations are attributed to the different sample masses used during volumetric measurements within the pycnometer where it is known that lower samples volumes lead to higher error values.

Table 4-2. Measured bulk densities (ρ) of solid samples, including both averages (ρ_{ave}) and standard deviations (ρ_{stdev}, $\pm 1\sigma$) from 10 separate volume measurements.*

Set	Sample ID	ρ_{ave} (g/cm^3)	ρ_{stdev} (g/cm^3)
A	Fe-P	2.9618	0.0042
B	Zn-Bi-Si	7.0257	0.0457
	Zn-Bi-Si-10ERV3-Q	6.5453	0.0396
	Zn-Bi-Si-10ERV3-F	6.7880	0.0378
C	Zn-Bi-B-1	4.7241	0.0042
	Zn-Bi-B-1-10ERV3-Q	4.3240	0.0086
	Zn-Bi-B-1-10ERV3-F	4.4144	0.0218
D	Zn-Bi-B-2	7.3611	0.0120
	Zn-Bi-B-2-10ERV3-Q	6.6231	0.0171
	Zn-Bi-B-2-10ERV3-F	7.1595	0.0742
E	Mo-Bi-Te-1	5.4732	0.0149
	Mo-Bi-Te-1-10ERV3-Q	4.9121	0.0119
	Mo-Bi-Te-1-10ERV3-F	5.0442	0.0191
F	Mo-Bi-Te-2	5.6227	0.0062
	Mo-Bi-Te-2-10ERV3-Q	4.9835	0.0046
	Mo-Bi-Te-2-10ERV3-F	5.1233	0.0243
G	Mo-Bi-Te-3	5.9550	0.0099
	Mo-Bi-Te-3-10ERV3-Q	5.1645	0.0084
	Mo-Bi-Te-3-10ERV3-F	5.3343	0.0205

*The Fe-P-O samples were not measured here because they were run in alumina crucibles which remained attached to the samples after the heat treatments

4.4 XRD Data

The Fe-P base glass remains amorphous after slow cooling, while the addition of ERV3 salt led to partial crystallization as shown in Figure 4-3. Slow cooled sample added with 10 mass% of ERV3 salt was observed with $LiFeP_2O_7$. Crystallization was more noticeable in slow cooled sample added with 20 mass% of ERV3 salt and the primary crystalline phases are $LiFeP_2O_7$, $KFeP_2O_7$, and $Li_4P_2O_7$. Other minor phases including $NaPO_3$, $NaFeP_2O_7$, CeFePO, and Fe_3O_4 are not labeled.

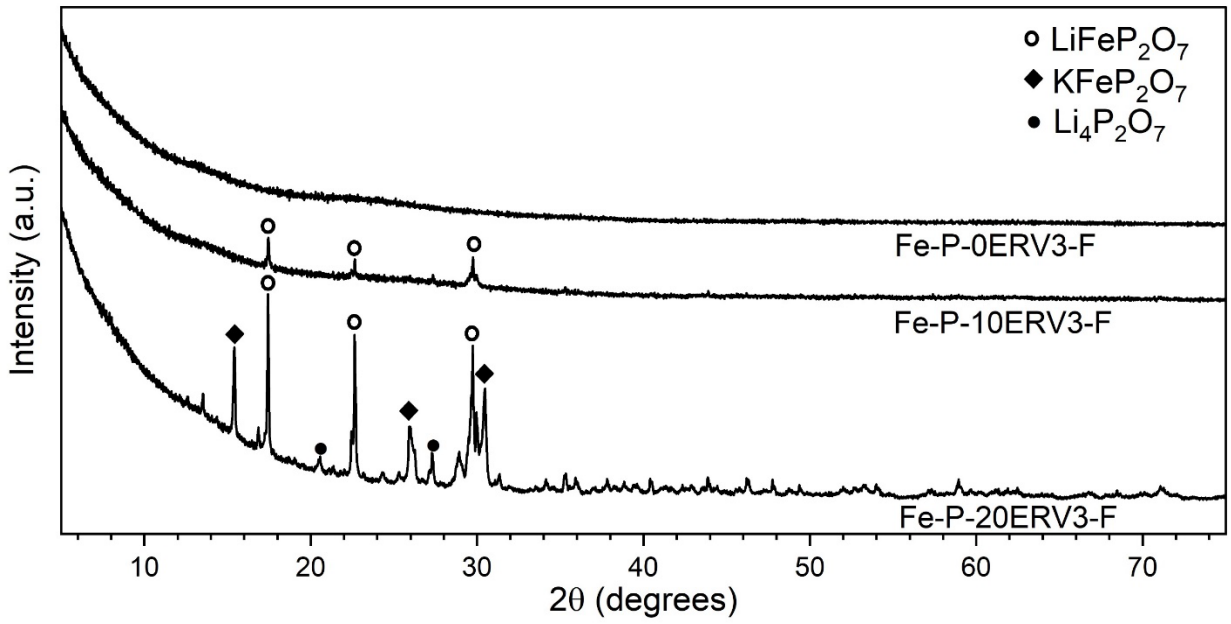

Figure 4-3. XRD of $40Fe_2O_3$-$60P_2O_5$ samples. Scans are labeled with the base glass composition along with salt addition and heat treatment.

For the ZnO-Bi_2O_3-B_2O_3/SiO_2 and MoO_3-Bi_2O_3-TeO_2 systems, all base glasses and samples with salt addition that were fast-cooled were X-ray amorphous except for the fast-cooled 25ZnO-$50Bi_2O_3$-$25B_2O_3$ sample with 10 mass% ERV3, which primarily formed $KCl(BiBO_3)_4$ (Figure 4-4). Crystallization was more prevalent in the slow-cooled samples and various types of crystalline phases were observed, including Bi_2SiO_5 and δ-Bi_2O_3 in 20ZnO-$40Bi_2O_3$-$40SiO_2$ (Figure 4-5), β-Bi_2O_3 in 25ZnO-$50Bi_2O_3$-$25B_2O_3$, $Mo_{0.15}Bi_{0.85}O_{1.725}$ and/or $Bi_{0.33}Te_{0.67}O_{1.835}$ in $20MoO_3$-$10Bi_2O_3$-$70TeO_2$ (see Table 4-3).

Table 4-3. Summary of XRD results from powdered samples with and without 10 mass% ERV3.

Glass composition	XRD results		
	Without ERV3	With 10 mass% ERV3 (fast cooled)	With 10 mass% ERV3 (slow cooled)
20ZnO-$40Bi_2O_3$-$40SiO_2$	Amorphous	Amorphous	Partially crystalline
25ZnO-$15Bi_2O_3$-$60B_2O_3$	Amorphous	Amorphous	Amorphous
25ZnO-$50Bi_2O_3$-$25B_2O_3$	Amorphous	Partially crystalline	Partially crystalline
$20MoO_3$-$2.5Bi_2O_3$-$77.5TeO_2$	Amorphous	Amorphous	Amorphous
$20MoO_3$-$5Bi_2O_3$-$75TeO_2$	Amorphous	Amorphous	Amorphous
$20MoO_3$-$10Bi_2O_3$-$70TeO_2$	Amorphous	Amorphous	Partially crystalline

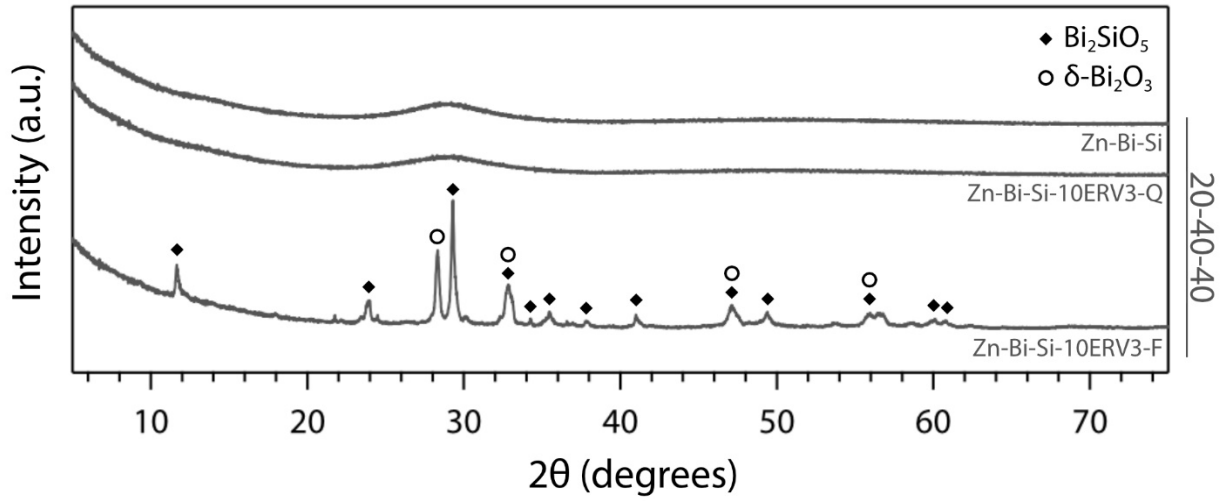

Figure 4-4. XRD of $20ZnO\text{-}40Bi_2O_3\text{-}40SiO_2$ samples. Scans are labeled with the base glass composition in mol% along with salt addition and heat treatment.

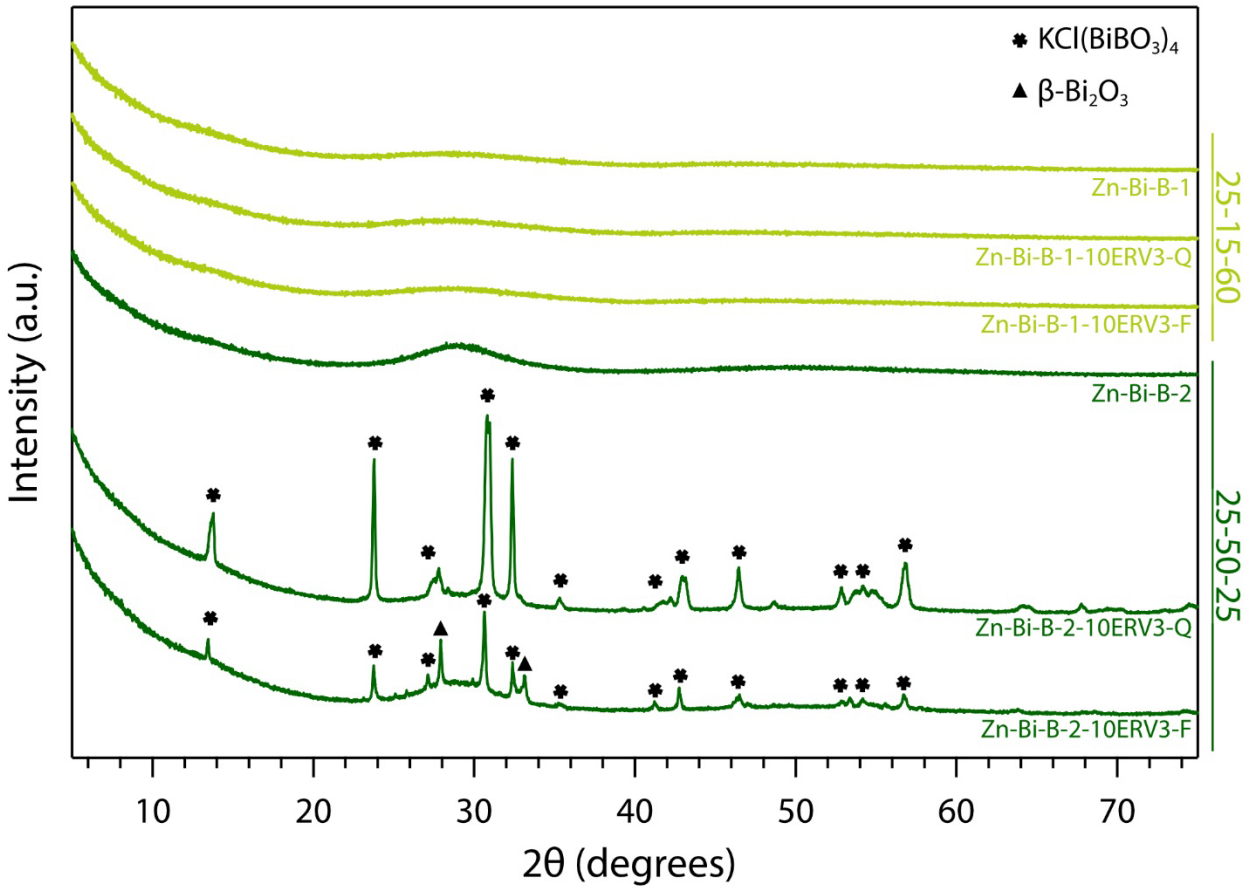

Figure 4-5. XRD of $ZnO\text{-}Bi_2O_3\text{-}B_2O_3$ samples. Scans are labeled with the base glass composition in mol% along with salt addition and heat treatment.

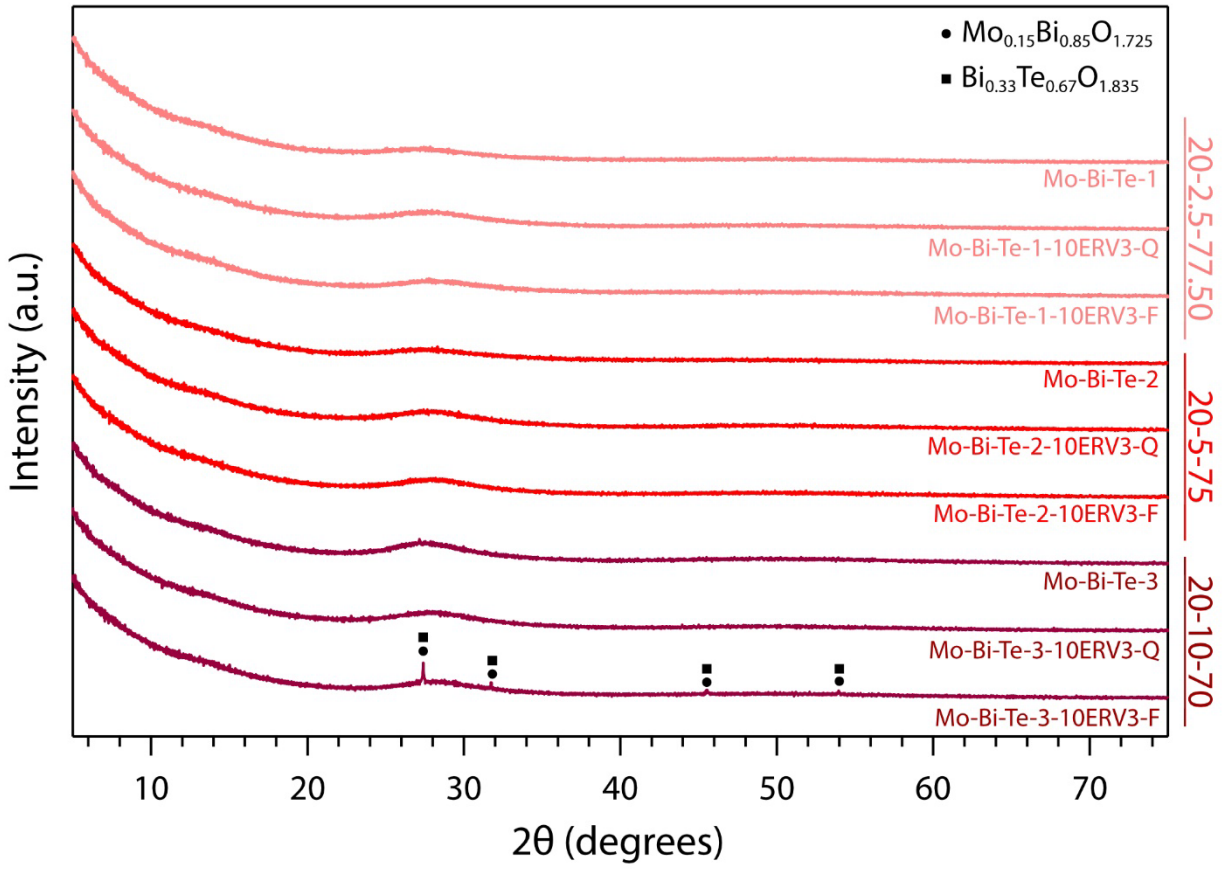

Figure 4-6. XRD of MoO_3-Bi_2O_3-TeO_2 samples. Scans are labeled with the base glass composition in mol% along with salt addition and heat treatment. Crystalline phases were only detected in the 20MoO_3-10Bi_2O_3-70TeO_2 with 10 mass% ERV3 slow-cooled sample.

4.5 SEM-EDS Data

Powder samples were examined by EDS to acquire the overall elemental composition for each of the salt loaded glasses, and the data is provided in Table 4-4. These values provide both the average and standard deviation values in mass%. Elements from both the base glass components and from the ERV3 salt are analyzed. The slight difference in the concentration of glass forming elements (e.g., Zn) between fast-cooled samples and slow-cooled samples may indicate the heterogeneity of salt-loaded glasses after different heat-treatment methods. Such compositional heterogeneity was also observed for the salt elements (e.g., K and Na), making it difficult to determine the actual retention level of Cl within the samples. Nevertheless, the Cl concentration was detected to be lower in the slow-cooled samples than in the fast-cooled samples for all salt-loaded glasses. This suggests that the slow-cooled samples suffered greater loss of Cl from volatilization due to longer heat-treatment time than the fast-cooled samples. Solid sample sections were mounted in epoxy, polished and coated with Ir for SEM-EDS. Microstructure of the samples with ERV3 additions were examined by BSE and EDS mapping to analyze the element partition among different phases.

Table 4-4. Average composition of powdered samples measured by SEM-EDS. “HT” denotes. Note that the values reported include averages with standard deviations (±1σ) below each.

Sample ID	Measured Values (mass%)											
	Zn	Bi	Si	Mo	Te	Cl	Na	K	Cs	Sr	Ce	Nd
Zn-Bi-Si-10ERV3-Q	3.08 ± 0.18	71.78 ± 0.20	4.08 ± 0.02	-	-	0.73 ± 0.02	1.65 ± 0.09	0.26 ± 0.02	0.05 ± 0.04	0.00 ± 0.00	0.38 ± 0.06	0.37 ± 0.10
Zn-Bi-Si-10ERV3-F	5.83 ± 0.43	68.73 ± 0.75	3.92 ± 0.07	-	-	0.49 ± 0.02	1.61 ± 0.05	0.20 ± 0.01	0.08 ± 0.05	0.00 ± 0.00	0.40 ± 0.07	0.29 ± 0.08
Zn-Bi-B-1-10ERV3-Q	9.99 ± 0.28	47.23 ± 0.14	-	-	-	0.66 ± 0.01	3.94 ± 0.15	2.17 ± 0.04	0.55 ± 0.07	0.25 ± 0.02	0.42 ± 0.06	0.40 ± 0.09
Zn-Bi-B-1-10ERV3-F	10.38 ± 0.19	47.60 ± 0.44	-	-	-	0.19 ± 0.02	4.04 ± 0.08	2.05 ± 0.02	0.51 ± 0.08	0.26 ± 0.04	0.49 ± 0.06	0.43 ± 0.10
Zn-Bi-B-2-10ERV3-Q	5.02 ± 0.26	69.87 ± 0.20	-	-	-	3.39 ± 0.13	1.77 ± 0.08	1.50 ± 0.09	0.10 ± 0.08	0.29 ± 0.04	0.39 ± 0.07	0.24 ± 0.09
Zn-Bi-B-2-10ERV3-F	7.63 ± 0.51	69.43 ± 0.70	-	-	-	0.38 ± 0.02	1.74 ± 0.07	0.10 ± 0.02	0.03 ± 0.04	0.25 ± 0.03	0.45 ± 0.09	0.30 ± 0.07
Mo-Bi-Te-1-10ERV3-Q	-	4.42 ± 0.04	-	10.82 ± 0.07	56.91 ± 1.33	1.68 ± 0.02	0.48 ± 0.04	2.12 ± 0.03	1.60 ± 0.10	0.22 ± 0.02	0.73 ± 0.04	0.14 ± 0.04
Mo-Bi-Te-1-10ERV3-F	-	5.52 ± 0.10	-	10.80 ± 0.08	61.73 ± 0.47	0.66 ± 0.05	0.32 ± 0.02	2.14 ± 0.01	1.54 ± 0.04	0.15 ± 0.01	0.69 ± 0.04	0.16 ± 0.04
Mo-Bi-Te-2-10ERV3-Q	-	8.93 ± 0.08	-	10.51 ± 0.04	55.64 ± 0.33	1.91 ± 0.02	0.36 ± 0.03	2.13 ± 0.01	1.67 ± 0.06	0.21 ± 0.03	0.81 ± 0.05	0.16 ± 0.05
Mo-Bi-Te-2-10ERV3-F	-	10.85 ± 0.04	-	10.60 ± 0.13	57.54 ± 0.48	0.48 ± 0.04	0.13 ± 0.14	2.12 ± 0.04	1.40 ± 0.03	0.09 ± 0.02	0.61 ± 0.03	0.22 ± 0.02
Mo-Bi-Te-3-10ERV3-Q	-	16.89 ± 0.78	-	10.04 ± 0.07	47.95 ± 0.90	2.33 ± 0.16	0.36 ± 0.03	2.04 ± 0.01	1.50 ± 0.06	0.20 ± 0.02	0.76 ± 0.08	0.19 ± 0.04
Mo-Bi-Te-3-10ERV3-F	-	18.92 ± 0.27	-	9.99 ± 0.04	47.44 ± 0.26	1.09 ± 0.03	0.38 ± 0.01	2.07 ± 0.02	1.51 ± 0.07	0.21 ± 0.02	0.81 ± 0.05	0.14 ± 0.05

4.5.1 Set-A: Fe-P

The maps from the center of the Fe-P-10ERV3 sample appeared homogenous (Figure 4-7). Several crystal phases are apparent in the Fe-P-20ERV3-F sample shown in Figure 4-8 and Figure 4-9. The K-rich locations in the EDS map are identified as the $KFeP_2O_7$ phase that was detected with XRD. Although Li cannot by detected with EDS, the K-deficient regions likely correspond to Li-containing phases. The bright areas in the BSE image match with the locations of Ce and Nd, indicating a separate phase. The maps also indicate Al from the alumina crucible used for heat treatment is present along interphase boundaries.

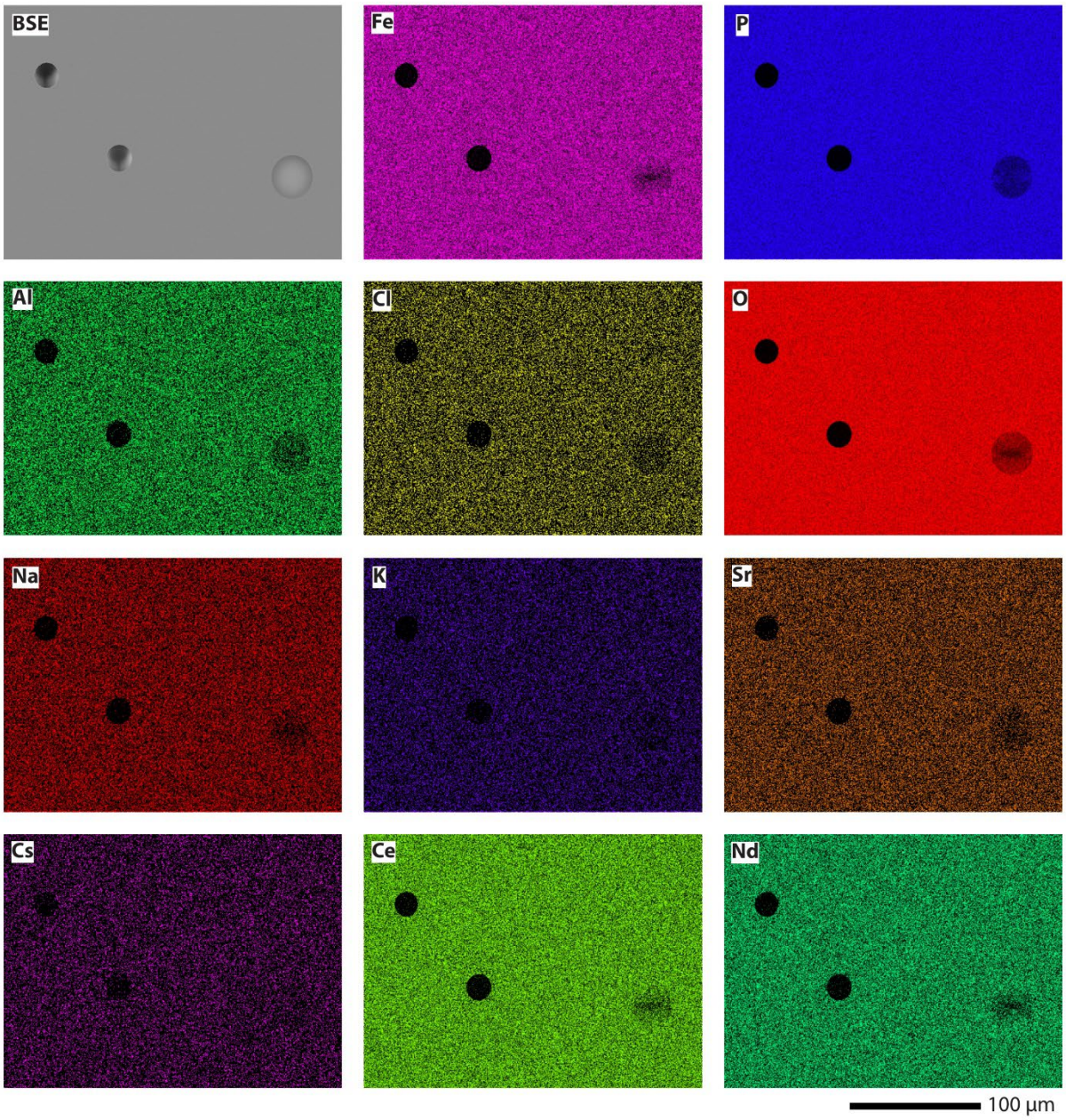

Figure 4-7 SEM-EDS maps of the Fe-P-10ERV3-F sample.

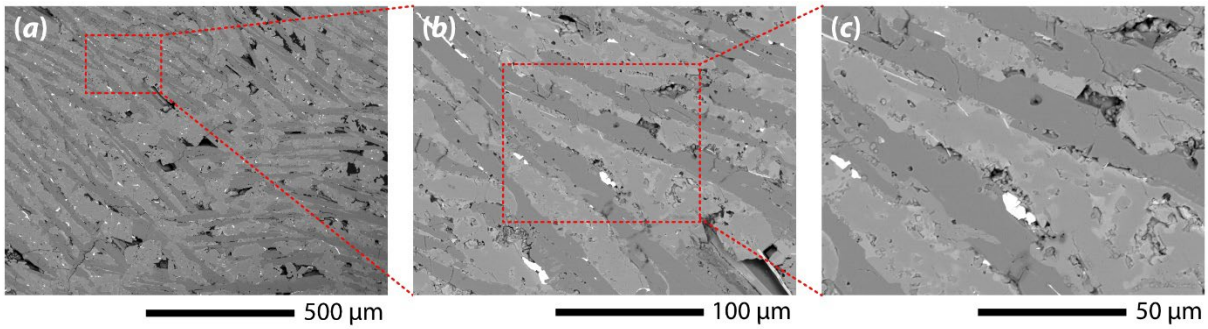

Figure 4-8. SEM-BSE micrographs of the Fe-P-20ERV3-F sample. Inset boxes mark magnified regions from the low-magnification region in (a), which is magnified in (b) and the box in (b) is magnified in (c).

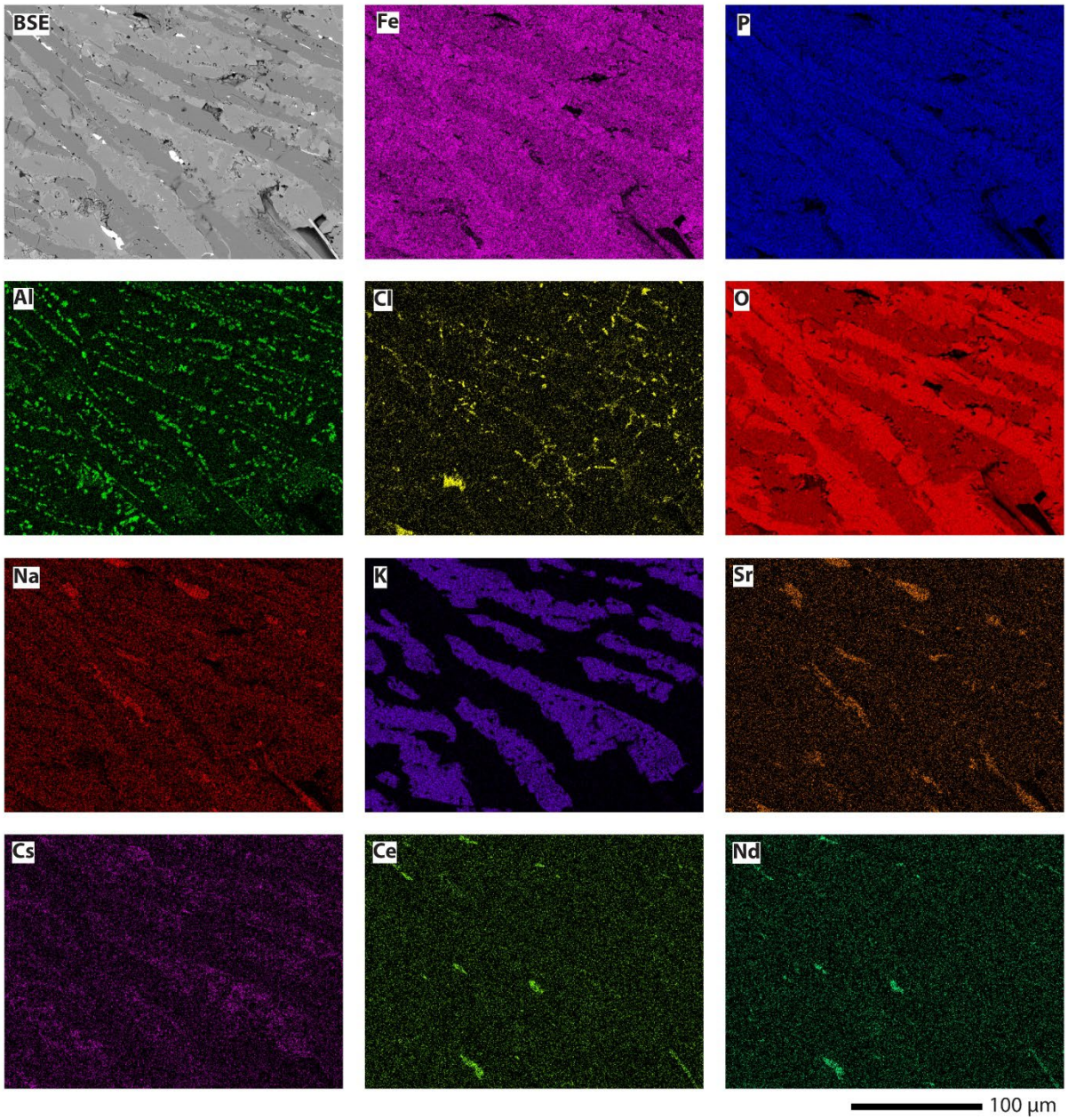

Figure 4-9. SEM-EDS maps of the Fe-P-20ERV3-F sample.

4.5.2 Set-B: Zn-Bi-Si

Figure 4-10 shows the needle like crystals formed close to the surface of the Zn-Bi-Si fast-cooled with 10 mass% ERV3 sample. These crystals are only observed on the surface of the sample, which is consistent with the previous observation of the surface pattern in Figure 4-2. These needle shaped crystals appear to be relatively rich in Bi, O, Si and Cl as shown in Figure 4-11, while the actual crystalline phase was not determined by XRD likely due to the minimal quantity. The phase is probably related to the Bi_2SiO_5 crystal confirmed in the slow-cooled sample and similar morphology on the Bi_2SiO_5 crystal was reported previously (Hammad et al. 2017). The crystal structure of Bi_2SiO_5 resembles the structure of bismuth oxychloride (BiOCl) (Ketterer and Freiburg 1986), which potentially explains the incorporation of the Cl into the needle-shape crystal. The $20ZnO\text{-}40Bi_2O_3\text{-}40SiO_2$ with 10 mass% ERV3 slow-cooled sample showed more extensive crystallization (see Figure 4-12). The EDS maps in Figure 4-13 reveal separation of bismuth and zinc into crystalline and residual glass phases, respectively. The Si concentration is highest in the residual glass phase (≈ 15 mass%), although it was also detected in crystalline portions of the sample, likely corresponding to the Bi_2SiO_5 phase determined with XRD. The EDS maps were unable to indicate the distribution of Sr, Cs, Ce, and Nd in the $20ZnO\text{-}40Bi_2O_3\text{-}40SiO_2$ with 10 mass% ERV3 samples due to the low concentrations of these elements.

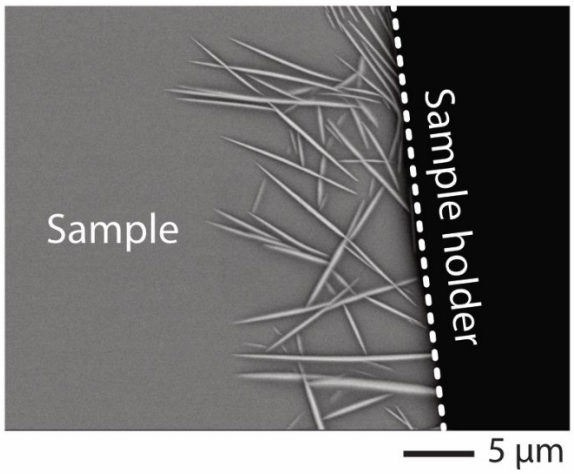

Figure 4-10. SEM-BSE micrograph of the Zn-Bi-Si-10ERV3-Q sample. The dashed line marks the edge of the sample.

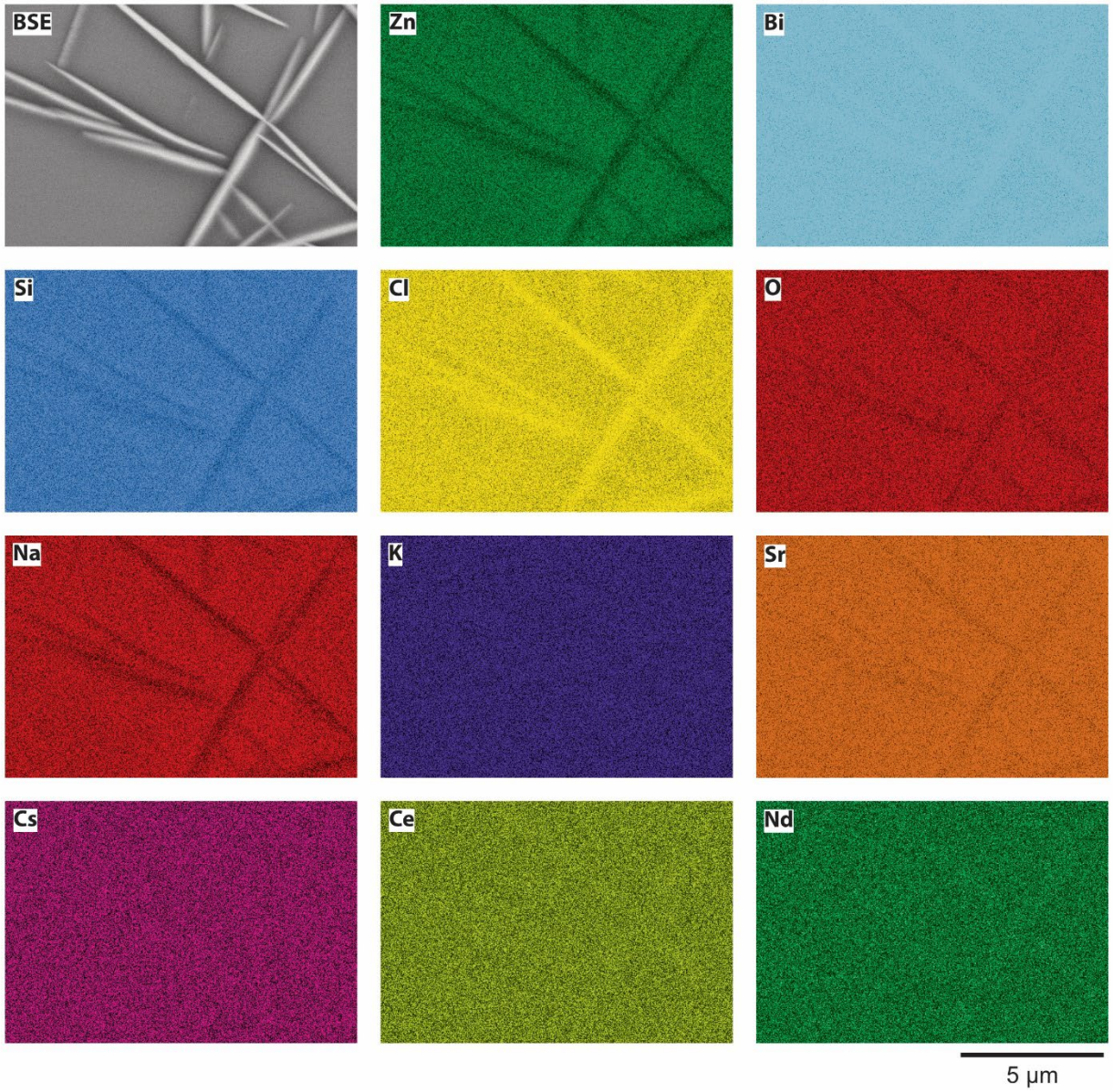

Figure 4-11. SEM-EDS maps of the Zn-Bi-Si-10ERV3-Q sample.

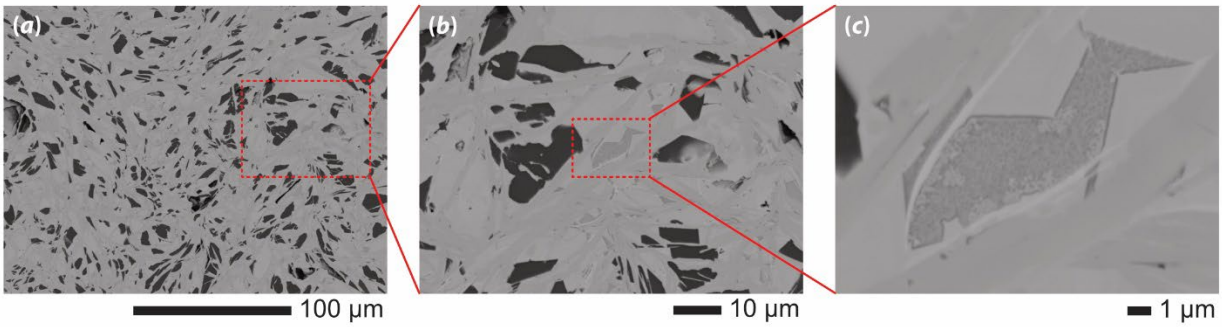

Figure 4-12. SEM-BSE micrographs of the Zn-Bi-Si-10ERV3-F sample. Inset boxes mark magnified regions.

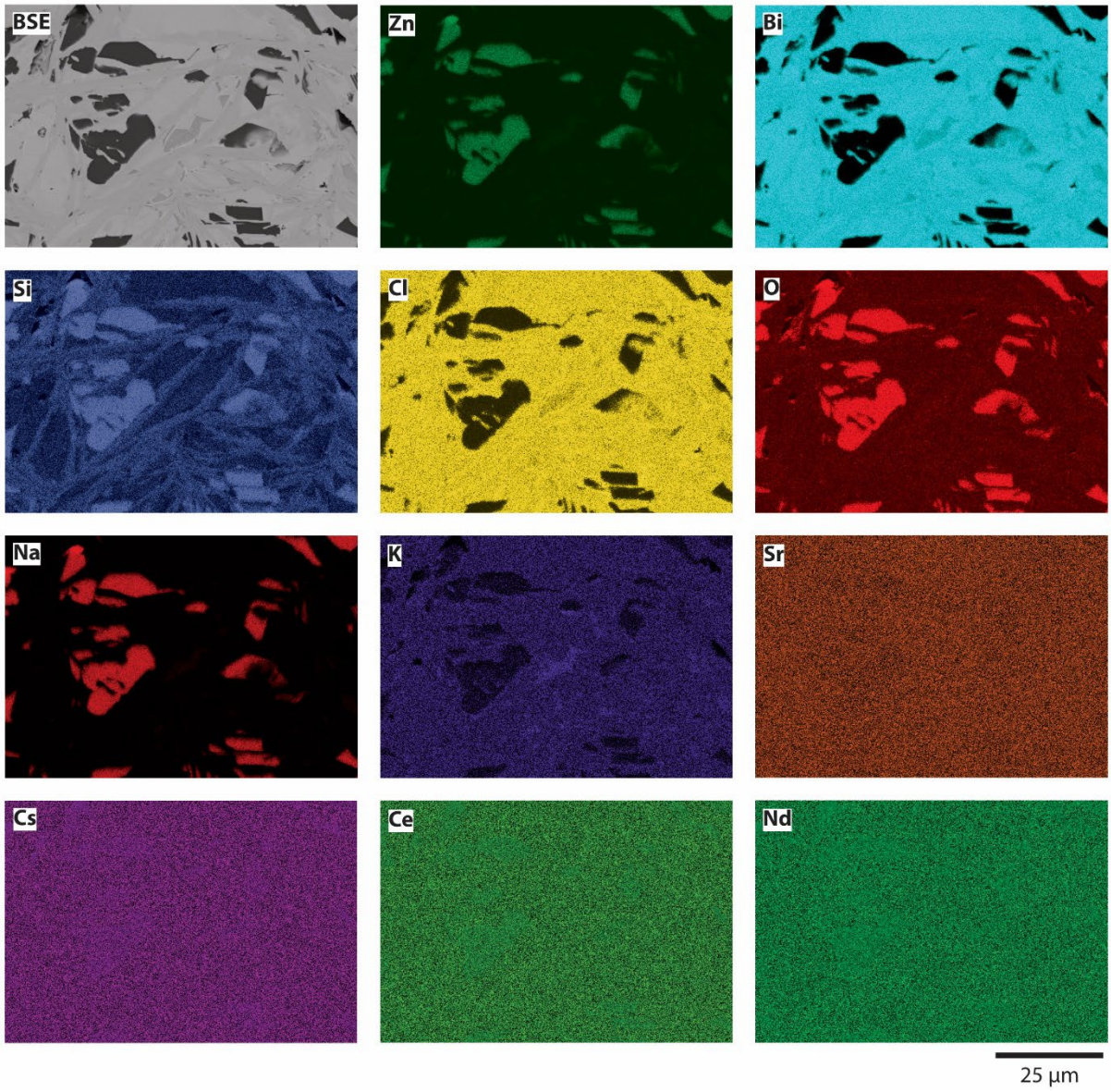

Figure 4-13. SEM-EDS maps of the Zn-Bi-Si-10ERV3-F sample.

4.5.3 Set-C: Zn-Bi-B-1

SEM-EDS of the Zn-Bi-B-1 fast-cooled and slow-cooled samples with ERV3 addition revealed homogeneous distribution of all components, as shown in Figure 4-14 and Figure 4-15, respectively. This is due to the amorphous nature of both samples.

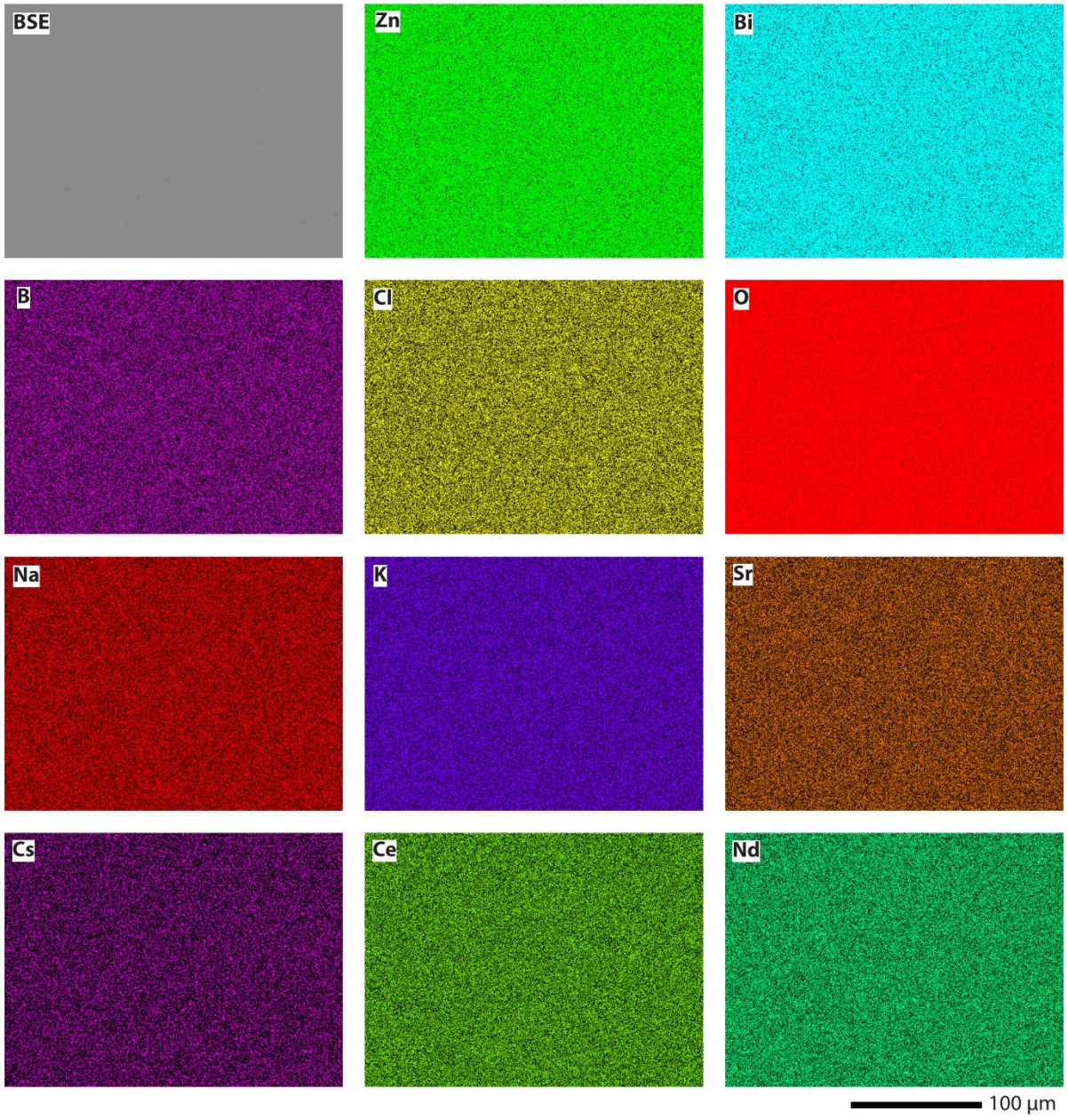

Figure 4-14. SEM-EDS maps of the Zn-Bi-B-1-10ERV3-Q sample.

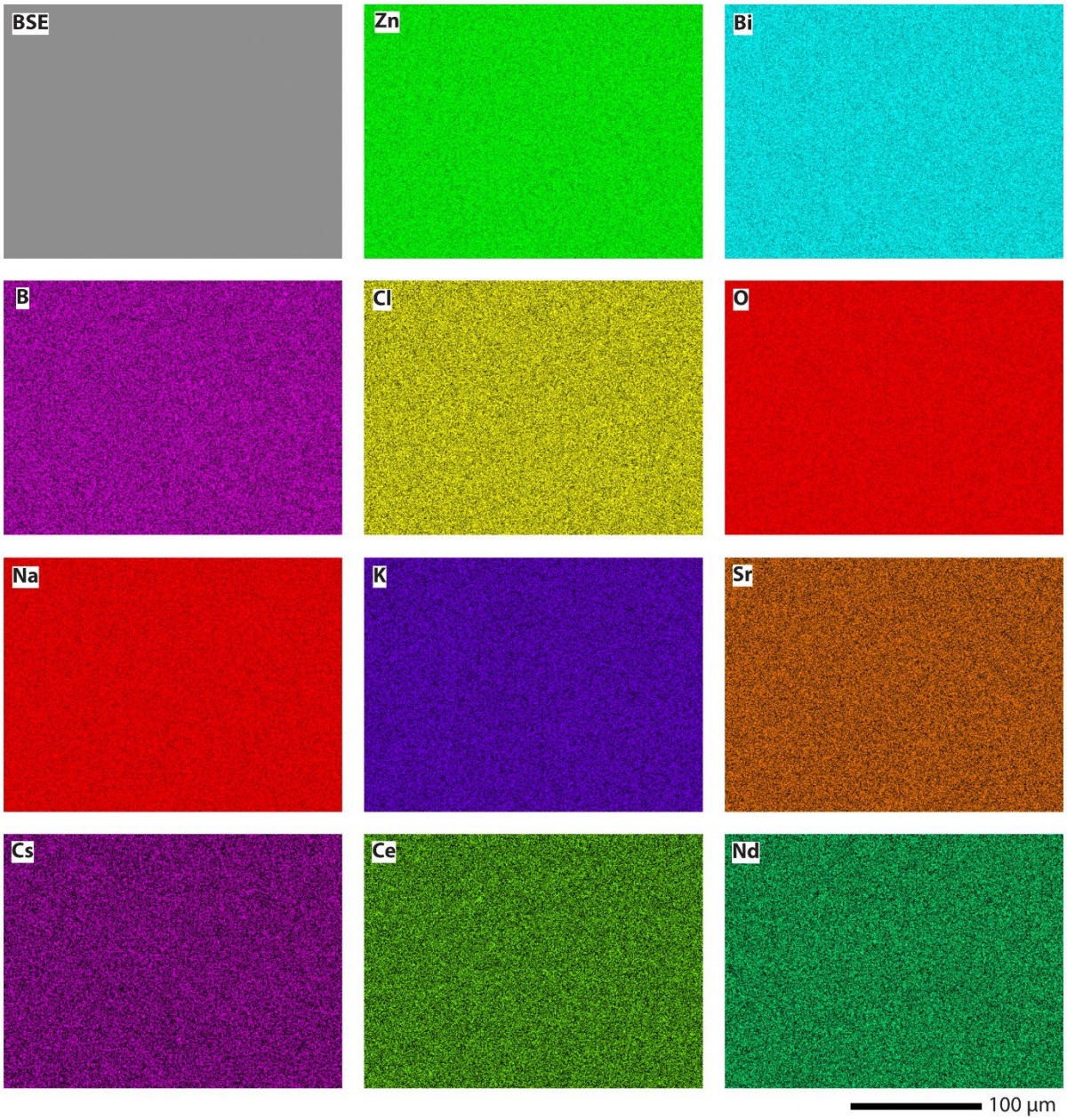

Figure 4-15. SEM-EDS maps of the Zn-Bi-B-1-10ERV3-F sample.

4.5.4 Set-D: Zn-Bi-B-2

As expected, based on XRD analysis results discussed previously, several crystalline phases were visible in both the fast- and slow-cooled samples of Zn-Bi-B-2 samples with 10 mass% ERV3. Figure 4-19 shows separation of Bi from the Zn glass phase. At least two different Bi phases are seen in Figure 4-19 and Figure 4-20. EDS maps indicate that the needle phase shown as middle grey have an increased Cl concentration, therefore likely corresponding to the $KCl(BiBO_3)_4$ phase determined with XRD. Additionally, the EDS maps of Ce and Nd indicate those elements are incorporated into the needle phase.

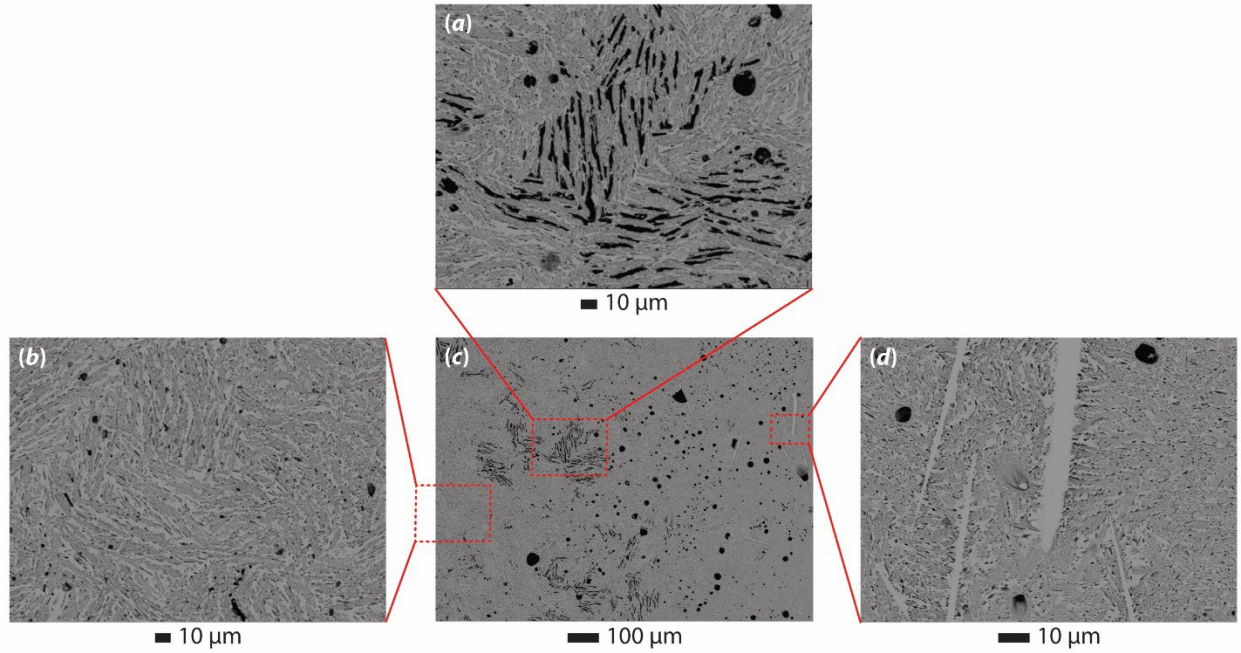

Figure 4-16. SEM-BSE micrographs of the Zn-Bi-B-2-10ERV3-Q sample. Inset boxes mark magnified regions. Dark regions are voids. The red lines show where each of the magnified regions in (a), (b), and (d) are shown in the lower-magnification region in image (c).

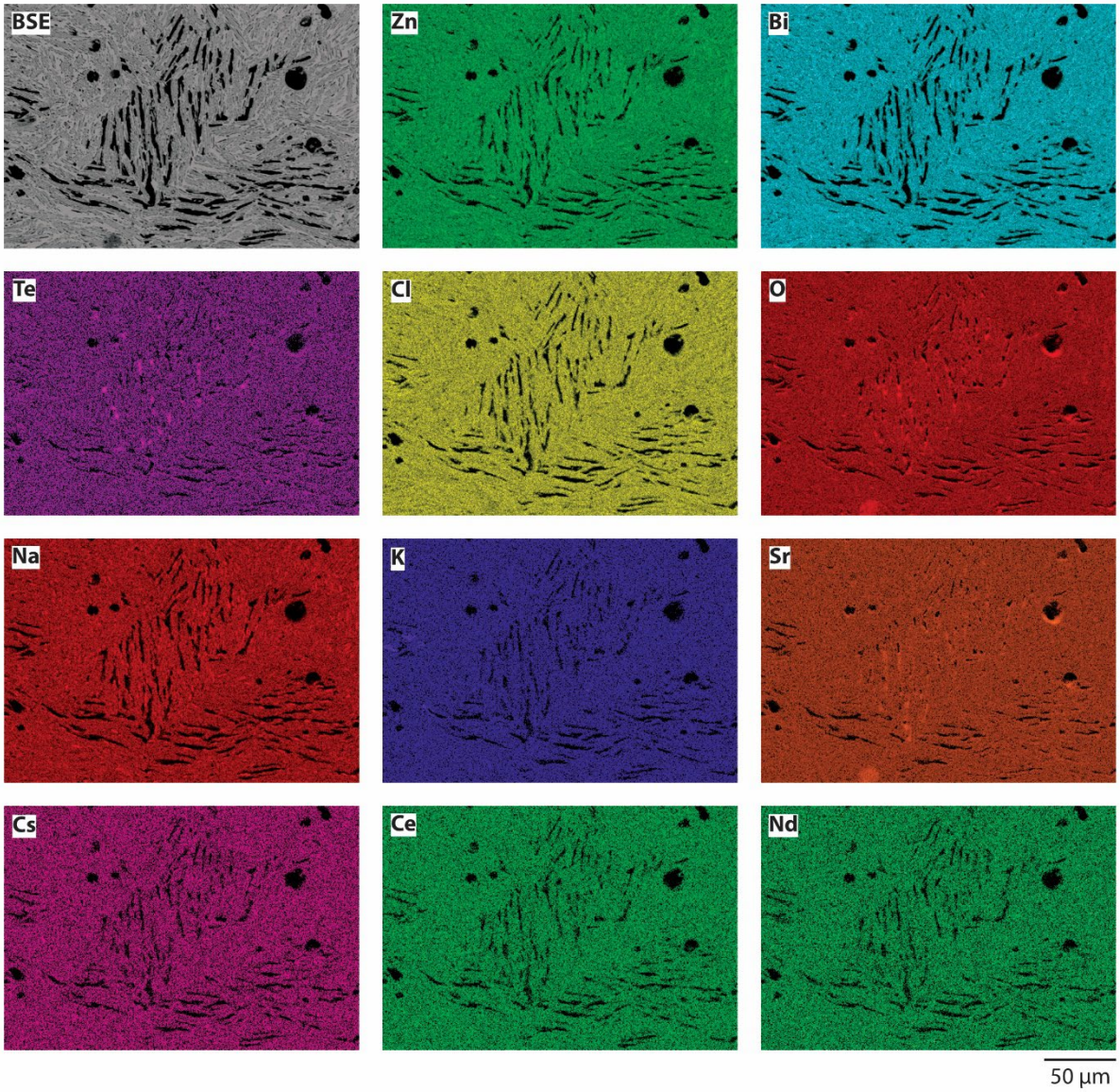

Figure 4-17. SEM-EDS maps of the Zn-Bi-B-2-10ERV3-Q sample. Black regions are voids.

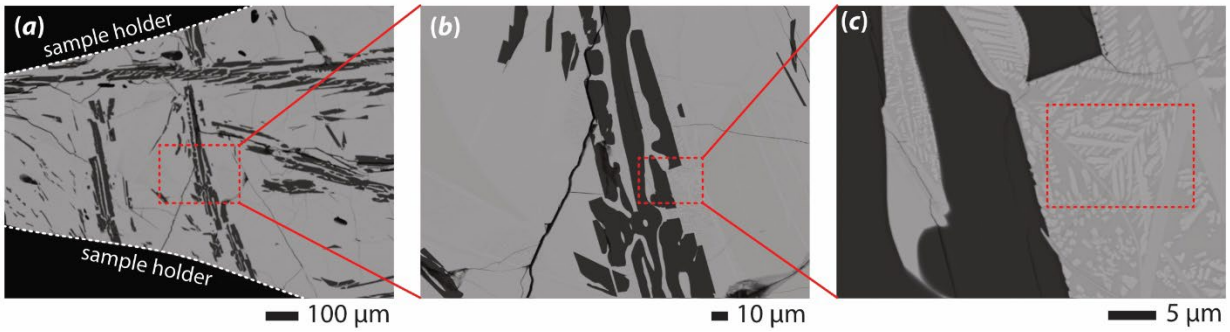

Figure 4-18. SEM-BSE micrographs of the Zn-Bi-B-2-10ERV3-F sample. Inset red boxes mark magnified regions. Dashed white lines in (a) indicate the edge of the sample. The inset box in (c) corresponds to SEM-EDS maps in Figure 4-20.

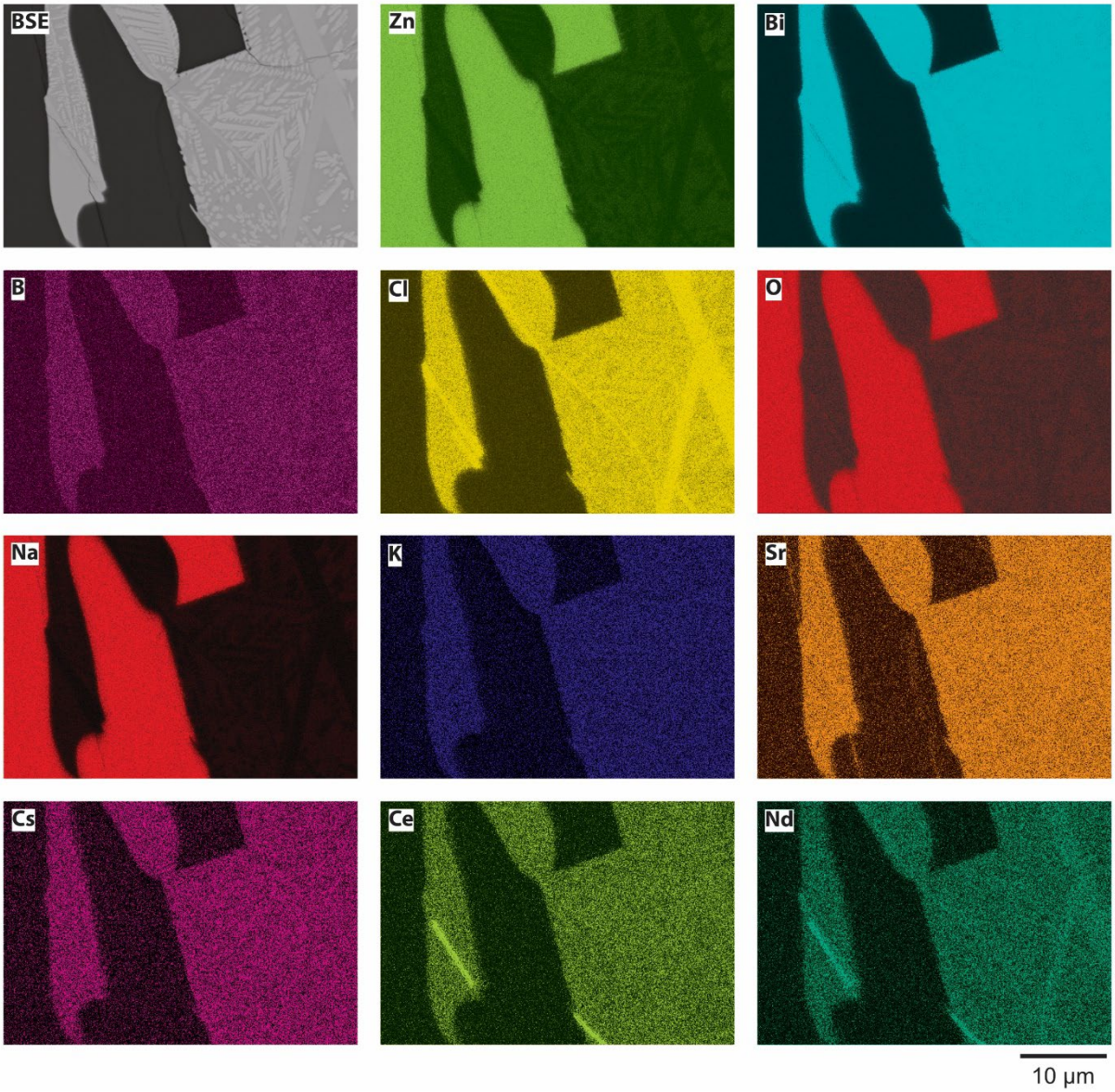

Figure 4-19. SEM-EDS maps of the Zn-Bi-B-2-10ERV3-F sample.

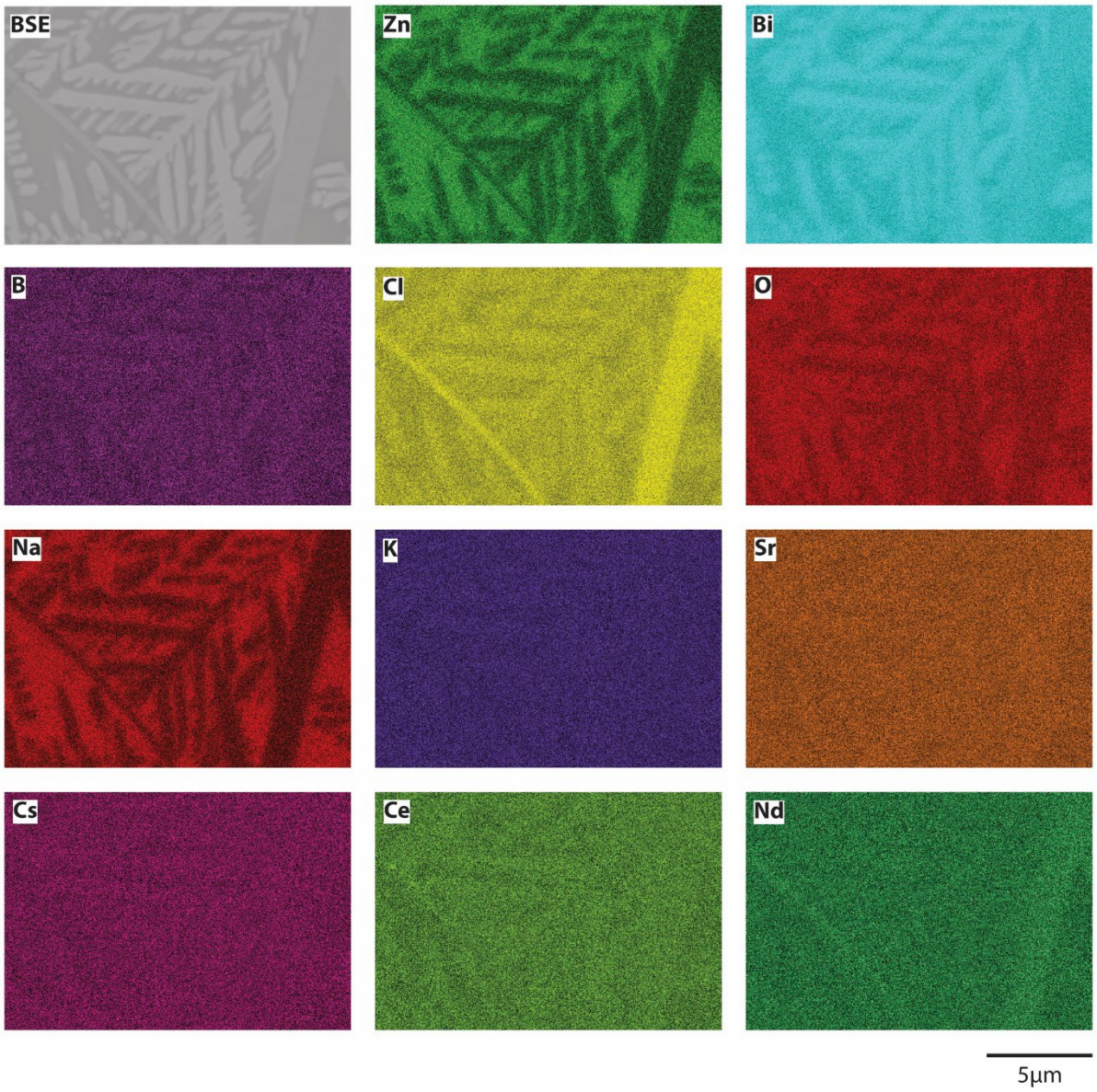

Figure 4-20. SEM-EDS maps of the Zn-Bi-B-2-10ERV3-F sample.

4.5.5 Set-E: Mo-Bi-Te-1

SEM-EDS of the Mo-Bi-Te-1 fast-cooled and slow-cooled samples with ERV3 addition revealed homogeneous distribution of all components, as shown in Figure 4-21 and Figure 4-22, respectively. This was due to the amorphous nature of both samples.

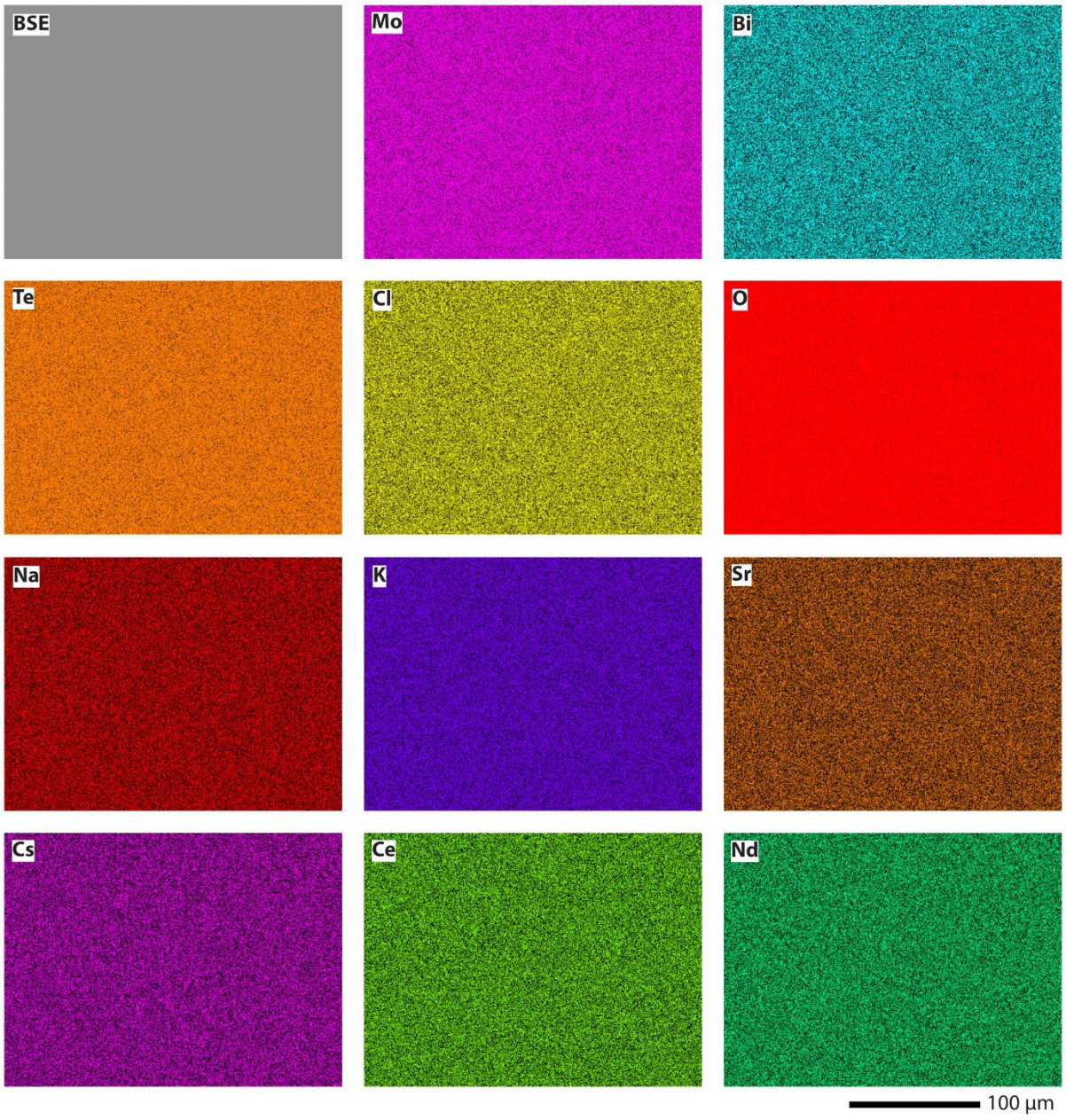

Figure 4-21. SEM-EDS maps of the Mo-Bi-Te-1-10ERV3-Q sample.

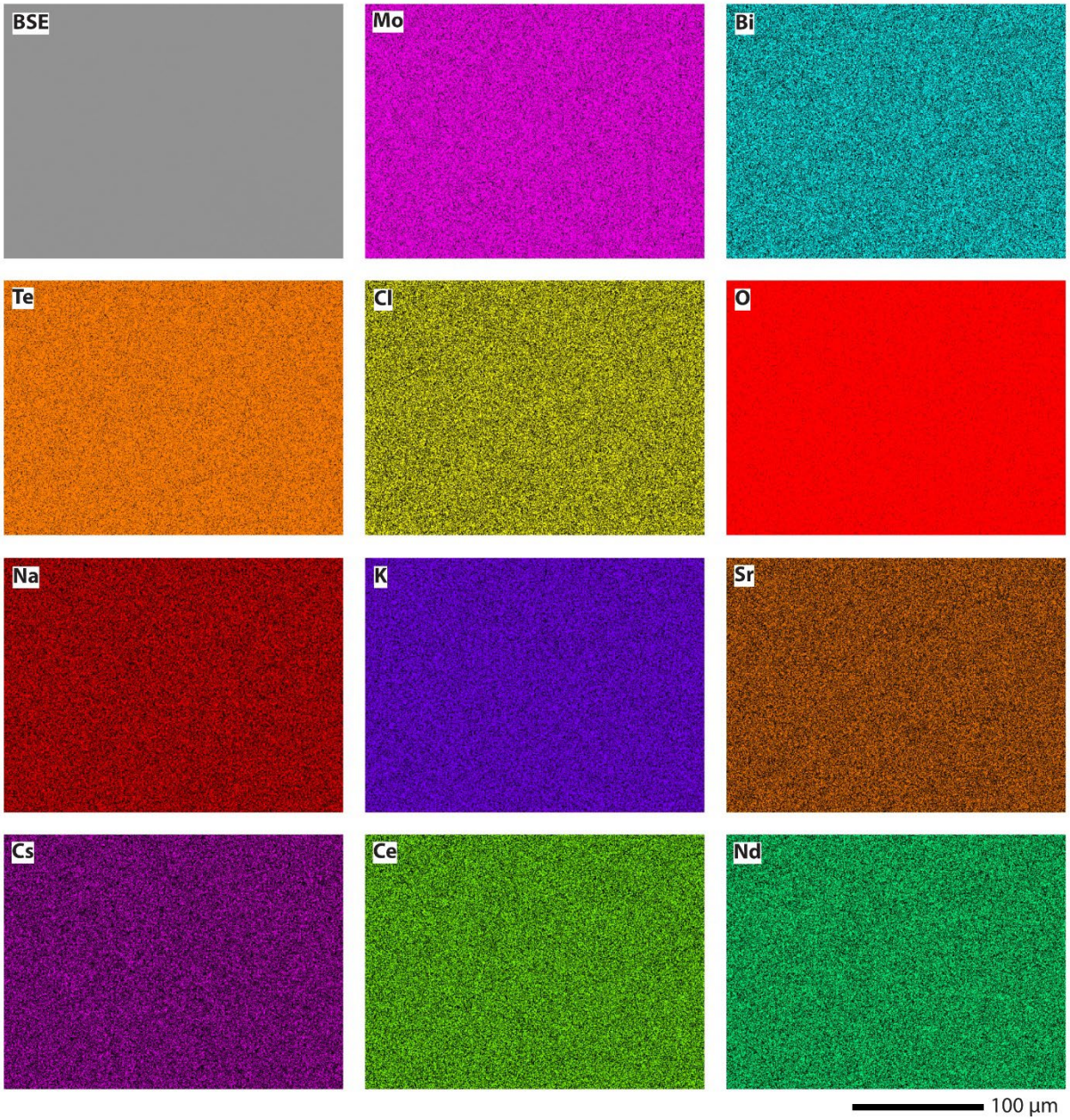

Figure 4-22. SEM-EDS maps of the Mo-Bi-Te-1-10ERV3-F sample.

4.5.6 Set-F: Mo-Bi-Te-2

SEM-EDS of the Mo-Bi-Te-2 fast-cooled and slow-cooled samples with ERV3 addition revealed homogeneous distribution of all components, as shown in Figure 4-23 and Figure 4-24, respectively. This was due to the amorphous nature of both samples.

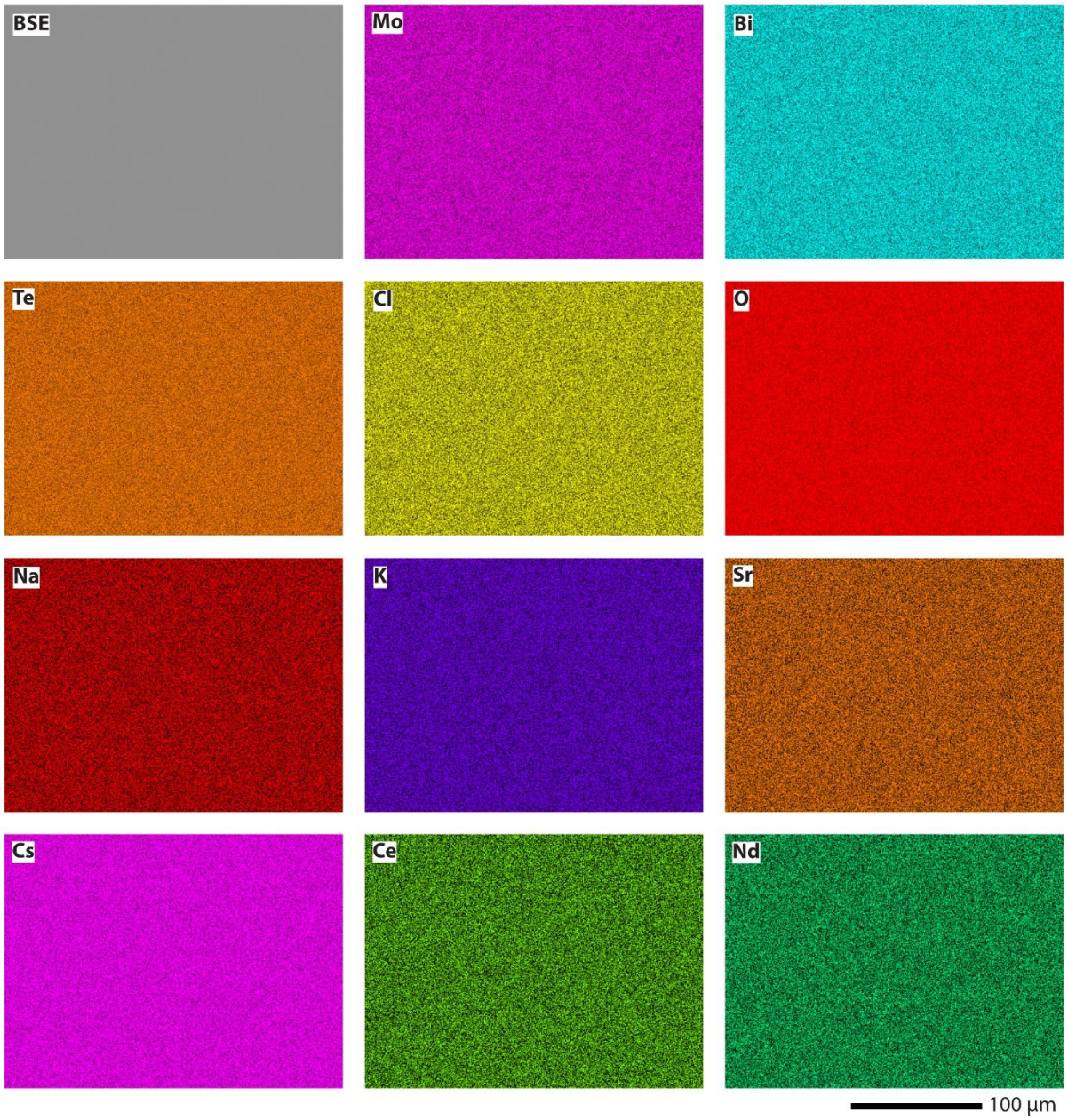

Figure 4-23. SEM-EDS maps of the Mo-Bi-Te-2-10ERV3-Q sample.

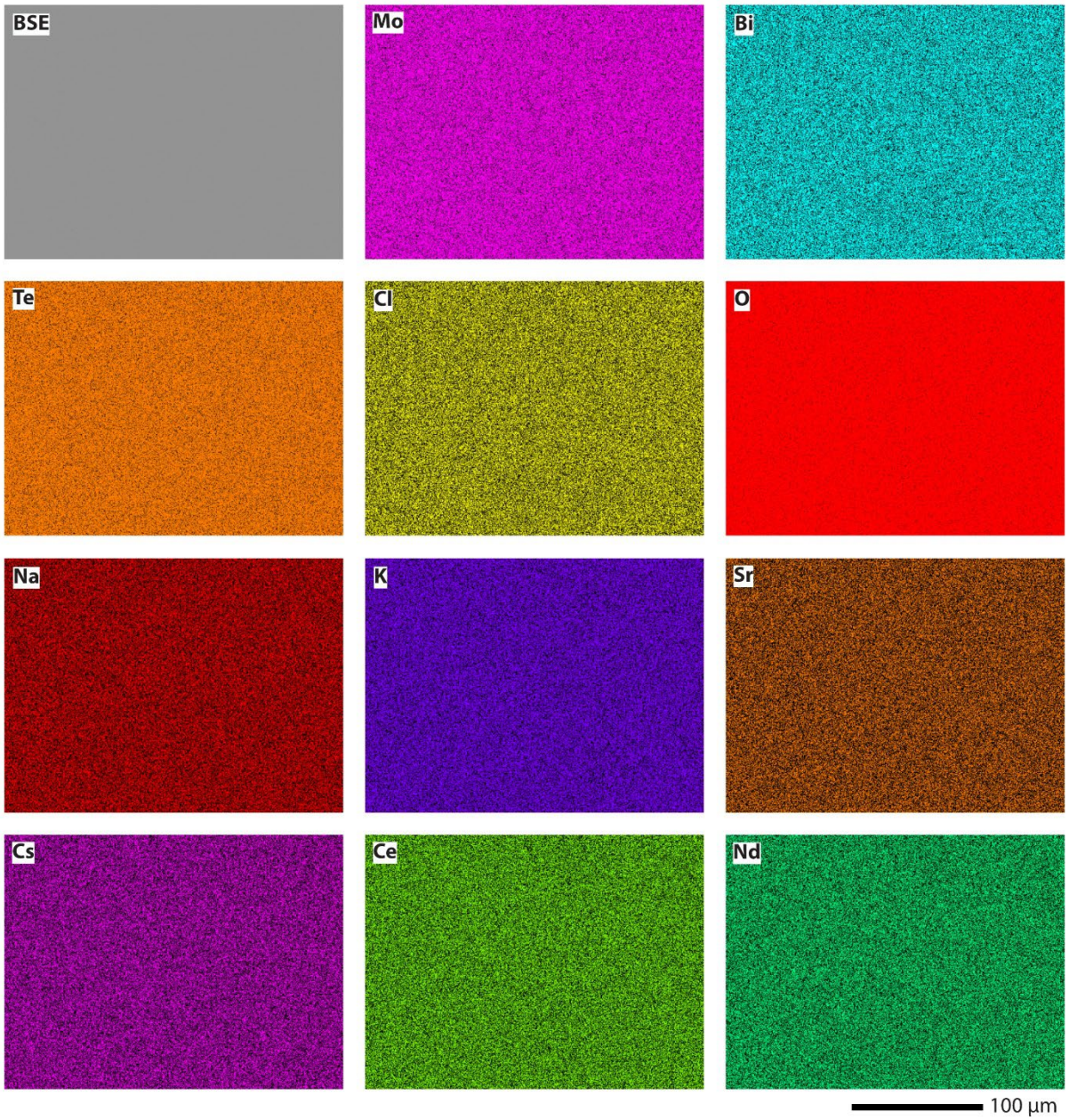

Figure 4-24. SEM-EDS maps of the Mo-Bi-Te-2-10ERV3-F sample.

4.5.7 Set-G: Mo-Bi-Te-3

SEM-EDS of the Mo-Bi-Te-3-ERV3-Q sample revealed homogeneous distribution of all components, as shown in Figure 4-25. Dendrites were observed close to the surface of Mo-Bi-Te-3-10ERV3-F in Figure 4-26. The dendrite composition was determined by EDS as rich in Te, Bi, and O, as shown in Figure 4-27, likely corresponding to the $Bi_{0.33}Te_{0.67}O_{1.835}$ phase determined by XRD. The region between dendrites has a reduced Bi concentration compared to the bulk of the sample.

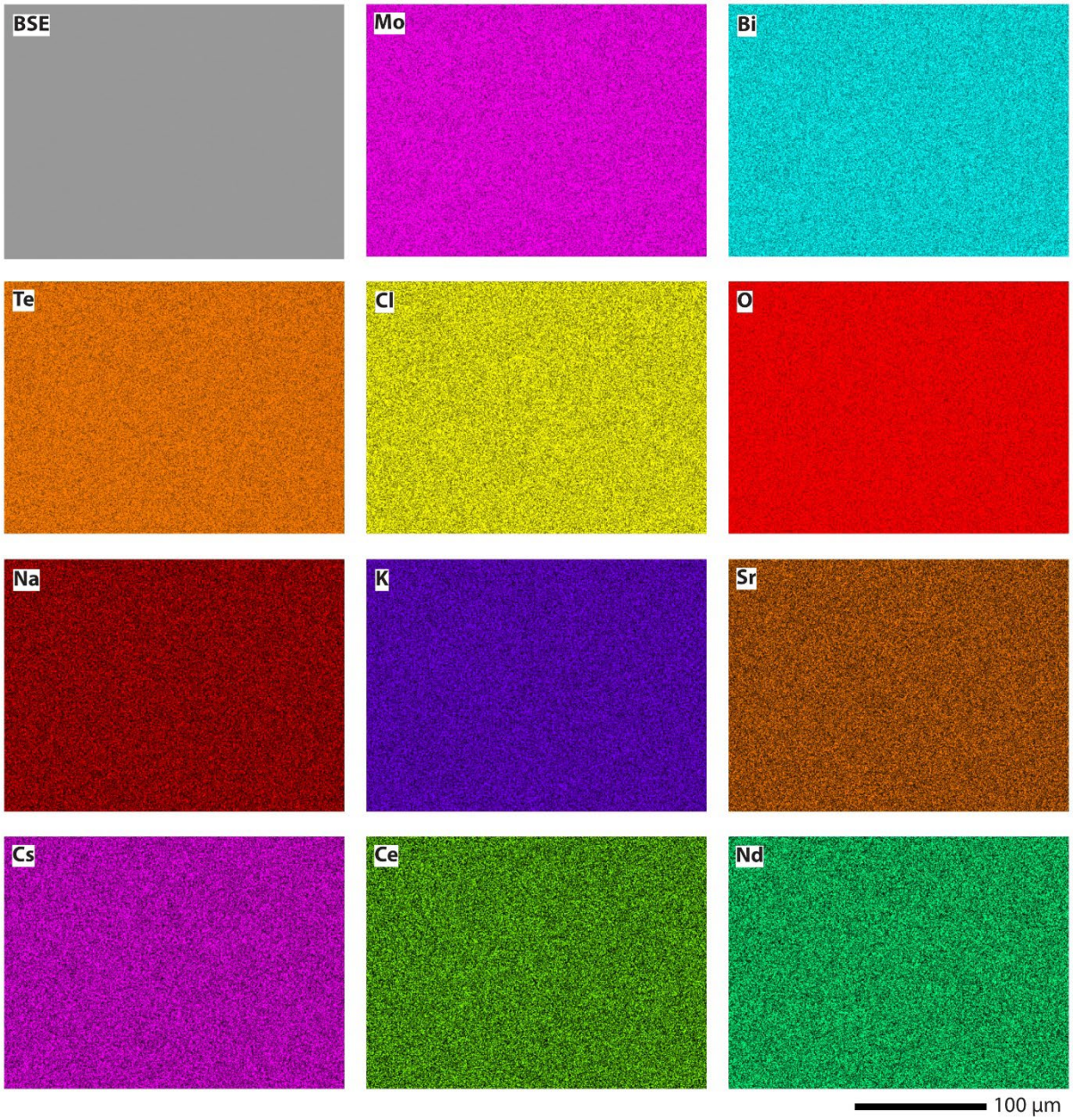

Figure 4-25. SEM-EDS maps of the Mo-Bi-Te-3-ERV3-Q sample.

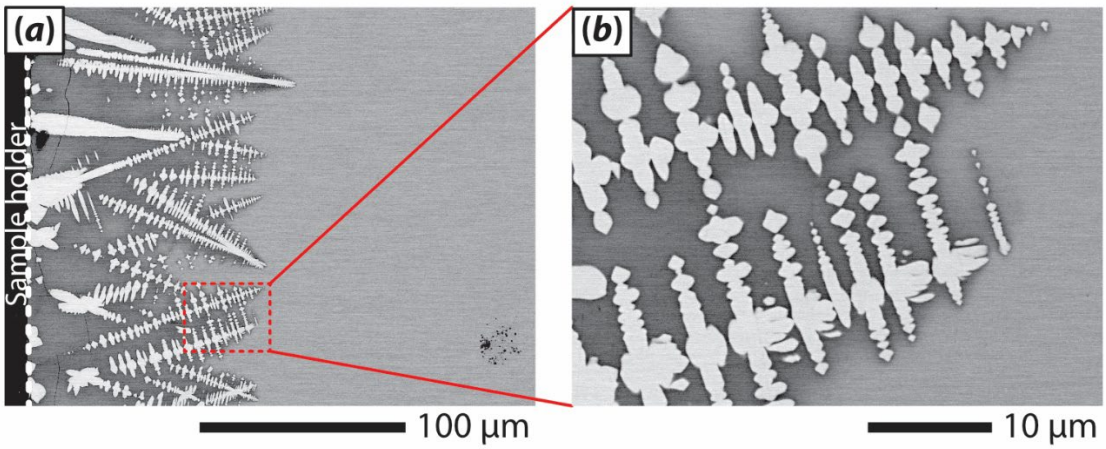

Figure 4-26. SEM-BSE micrographs of Mo-Bi-Te-3-10ERV3-F showing surface crystallization. The inset box in (a) marks the magnified region in (b). The white dashed line indicates the sample edge.

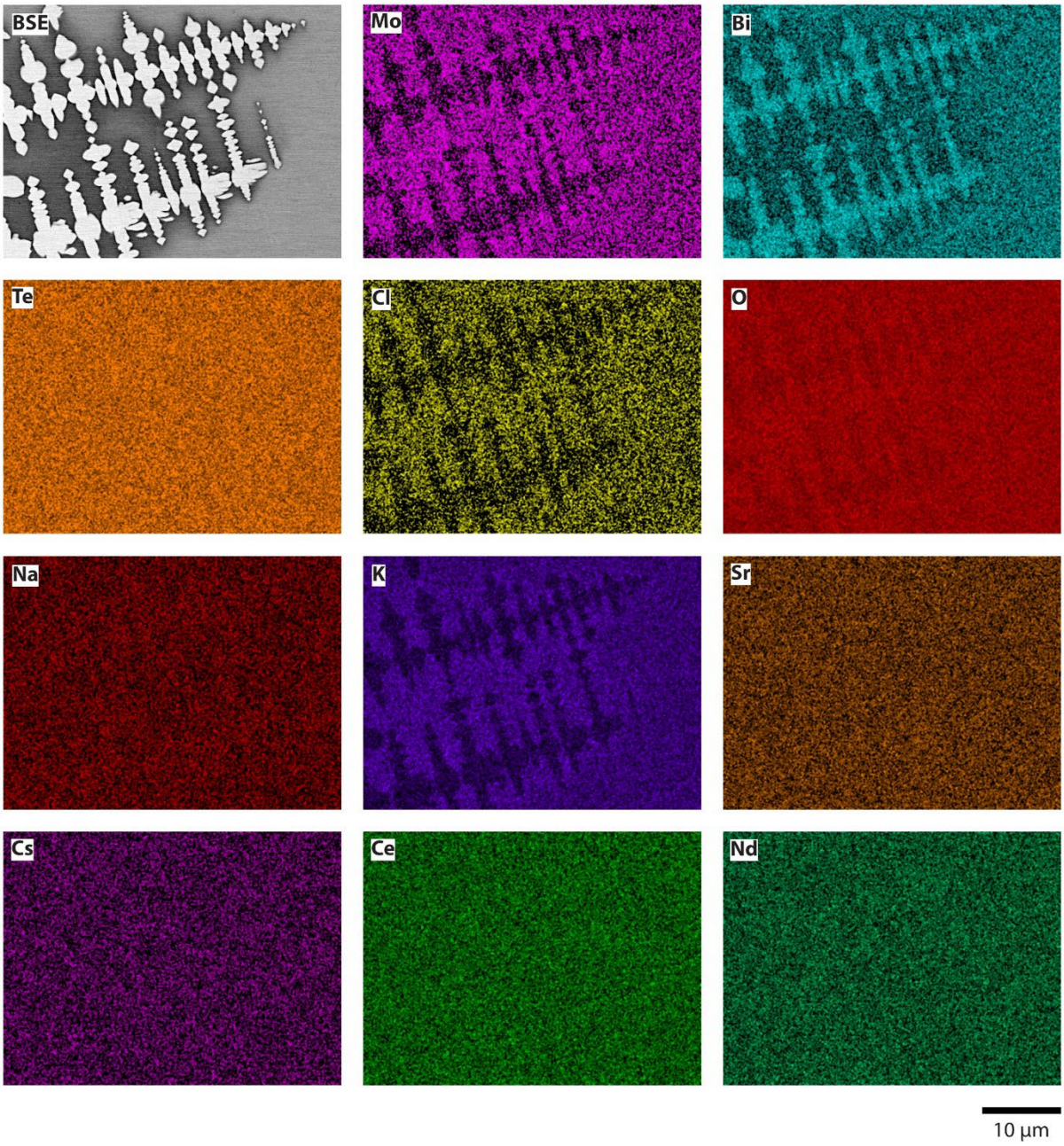

Figure 4-27. SEM/EDS maps of Mo-Bi-Te-3-10ERV3-F. This location comes from Figure 4-26.

5.0 Discussion of Results

Several glass systems have been examined on the feasibility of incorporating ERV3 salt. The chemistry and properties of the base glass and salt-loaded samples were characterized by various techniques. The binary $40Fe_2O_3$-$60P_2O_5$ glass was previously reported to host high-level waste (HLW) and low activity waste (LAW) with good chemical durability. In this study, the $40Fe_2O_3$-$60P_2O_5$ glass was test with different loading levels of the ERV3 (10 and 20 mass%). XRD results showed the Fe-P-10ERV3-F is lightly crystalized and the crystalline phases of lithium iron phosphate ($LiFeP_2O_7$) and Magnetite (Fe_3O_4) were detected. Fe-P-20ERV3-F is heavily crystalized with multiple alkaline phosphate ($NaPO_3$ and $Li_4P_2O_7$) and alkaline iron phosphate phases (e.g. $LiFeP_2O_7$ and $KFeP_2O_7$) formed during the furnace cooling process. Apparently, the higher salt loading of ERV3 introduces a greater amount of alkaline to facilitate the crystal formation. The mass fraction loss of the slow-cooled Fe-P glasses loaded with ERV3 appears to increase linearly with increasing amount of the ERV3 salt loading as shown in Figure 5-1. This may suggest the mass loss is mostly the result of the volatilized salt components during the furnace heat-treatment.

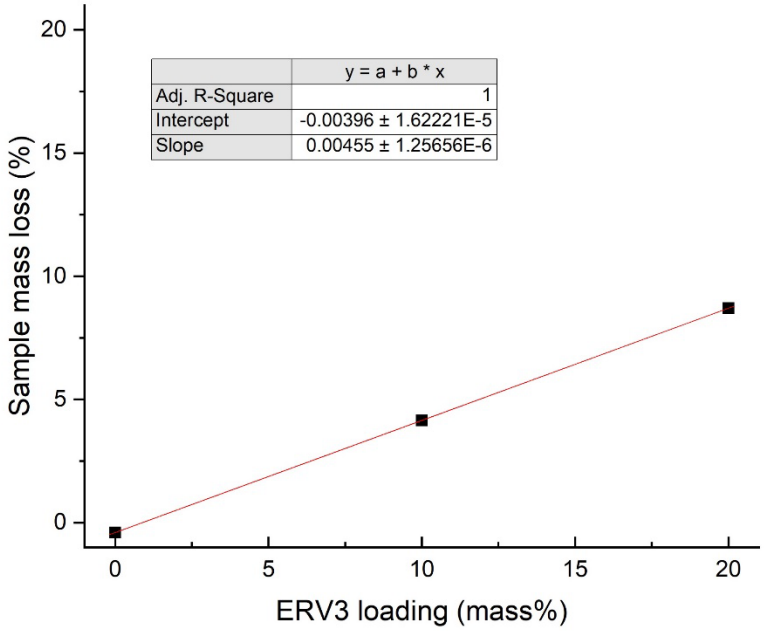

Figure 5-1. Mass fraction loss of slow cooled Fe-P glass loaded with different amounts of ERV3 salt.

The three compositions selected for ZnO-Bi_2O_3-B_2O_3/SiO_2 glasses were successfully fabricated using the conventional melt-quench method. However, different behavior was observed on the crystallization during cooling with the ERV3 salt addition. The $25ZnO$-$15Bi_2O_3$-$60B_2O_3$ glass showed great resistance to crystallization with 10 mass% of ERV3 under both fast- and slow-cooled conditions without any crystal formation. The potential homogeneous incorporation of salt is likely attributed to the excellent glass forming ability of the glass composition. For the $20ZnO$-$40Bi_2O_3$-$40SiO_2$ glass, the addition of ERV3 caused the slight devitrification of the fast cooled sample. Such effects became more pronounced for the slow cooled sample as evidenced by the apparent crystallization. The $25ZnO$-$50Bi_2O_3$-$25B_2O_3$ glass were heavily crystallized with ERV3 addition for both fast- and slow-cooled conditions, indicating the poor resistance to crystallization of the glass. The mass fraction loss of the slow cooled samples (e.g., 10.16% of $20ZnO$-$40Bi_2O_3$-

$40SiO_2$ and 9.87% of $25ZnO\text{-}15Bi_2O_3\text{-}60B_2O_3$) are close to the total addition of the ERV3 salt (10 mass%), indicating that the majority of the ERV3 could be volatilized during the furnace heat-treatment.

Good glass formation was confirmed for the $20MoO_3\text{-}xBi_2O_3\text{-}(80\text{-}x)TeO_2$ system with x =2.5 and 5 mol% by both visual apparency and XRD. These two glasses have shown good resistance to crystallization with the addition of ERV3 salt under both fast-cooling and slow-cooling heat-treatment methods. The $20MoO_3\text{-}10Bi_2O_3\text{-}70TeO_2$ glass showed no crystalline peaks by XRD but the cloudy suggests the fast-cooled glass could be phase-separated. With the addition of ERV3 salt, crystal formation was detected for the glass after slow-cooling heat-treatment. Regarding the total mass loss after heat-treatment, all three glasses showed similar values (Table 4-1) under the same heat-treatment condition, indicating the volatilization of salt components has less dependence on the glass composition than on the heat-treatment condition.

6.0 Summary and Conclusions

This work aimed to identify compositions with the potential to retain and immobilize salt waste from electrochemical processing, namely the LiCl-KCl electrorefiner salt wastes containing NaCl (from Na bond) as well as dissolved fission products after actinide and lanthanide drawdown. Based on a literature review, four primary glass systems were selected based on their documented glass-forming ability and salt loading potential: Fe_2O_3-P_2O_5, MoO_3-Bi_2O_3-TeO_2, ZnO-Bi_2O_3-SiO_2, and ZnO-Bi_2O_3-B_2O_3. Seven compositions within those four glass systems were identified as promising candidates to evaluate experimentally.

For the salt simulation, the ERV3 composition was selected, produced at ANL, and shipped to PNNL for experiments. Within the ERV3 salt simulant, large chunks of salt were present and differences in color indicated heterogeneity within the ERV3 salt from the salt synthesis process. Therefore, due to the heterogeneity in the ERV3, the exact salt composition added to each sample during synthesis varied in an uncontrollable fashion. This was discovered later at the stage of glass characterization after samples had been produced. Thus, losses due to volatilization of ERV3 components are not known and mass balance evaluation was difficult. However, the measured mass loss and composition after heating can provide an approximate ranking of halide retention of each glass system. Glass system sets **B** (Zn-Bi-Si), **C** (Zn-Bi-B-1), and **D** (Zn-Bi-B-2) lost the most mass after salt addition and furnace heat treatment, likely indicating that most of the salt volatilized during processing for these glasses. This may be caused by the inability of the system to retain the salt components, the parameters of the heat treatment (the high temperatures used), a combination of these conditions, or something else. Additionally, the Cl content as measured by SEM-EDS of powdered samples was lower in all slow-cooled samples compared to their fast-cooled counterparts, pointing to losses both during the high-temperature isothermal hold and during the cooling profile. Additional study of these compositions and their salt retentions would be aided by preparation of individual batches of salt waste simulants separately batched from anhydrous salt constituents for each sample, as opposed to using a pre-made, multi-component salt simulant. This would help ensure that the composition of each sample was known precisely and would help with mass balances, assessment of Cl retention, and assessment of fission product retention (and which fission products were not retained).

Analyses of the crystallinity, microstructure, and compositions of samples were performed with XRD and SEM-EDS. The base glass compositions were prepared with the melt-quench method and all were X-ray amorphous. Two samples were partially crystalline after the addition of 10 mass% ERV3 and preparation by melt quench. No crystalline phases were detected in the Zn-Bi-Si-10ERV3-Q sample with XRD, but SEM-EDS analysis revealed a needle-like phase at the surface that was relatively rich in Bi, O, Si and Cl. The Zn-Bi-B-2-10ERV3-Q contained $KCl(BiBO_3)_4$ phases that were detected with XRD. Crystallization was more apparent in samples that were slow cooled by heat treatment after ERV3 addition. SEM-EDS of Zn-Bi-B-2-10ERV3-F detected Ce, Nd, and Cl in the same regions, likely indicating the rare earths incorporate into the $KCl(BiBO_3)_4$ structure. Both fast-cooled samples that were partially crystalline were also partially crystalline after slow-cooling. Additionally, Mo-Bi-Te-3-10ERV3-F contained crystals at the surface that matched the structure of $Bi_{0.33}Te_{0.67}O_{1.835}$, confirmed by SEM-EDS detection of dendrites rich in Bi, Te, and O. In Fe-P samples, increased salt content caused more extensive crystallization. $LiFeP_2O_7$, $KFeP_2O_7$, and $Li_4P_2O_7$ were identified with XRD of the Fe-P-20ERV3-F sample. SEM-EDS revealed regions with additional phases, such as a Ce-rich and Nd-rich areas.

To finalize the dataset, PNNL is awaiting results from ANL to understand the chemical durability performances of these samples. With that data, the team will have a more comprehensive

overview of the true performance. The goal following this work would be to take the best-performing compositions from fiscal year (FY) 2025 and build upon this foundation to expand these compositions into FY2026 with (a) higher waste loadings (e.g., salt loadings other than 10 mass%) and/or (b) different heat treatment processes (e.g., lower heat-treatment temperatures, lower heat-treatment times) to evaluate opportunities to maximize salt retention in the final products.

7.0 Future Work

After considering the observed from this study, some things could be performed differently in a follow-up study to improve the progress of this work. The main limitations to the samples loaded with ERV3 salt were that the ERV3 salt simulant was heterogeneous. This made tracking the retention of Cl and fission product cations difficult both gravimetrically and by chemical analysis with EDS. Tracking was complicated by the fact that a large mole fraction of the ERV3 is Li, which cannot be easily mapped, i.e., it is not trackable with EDS and requires a different technique like secondary ion mass spectrometry (SIMS). Additionally, the sample sizes used for heat treatments within the current study were small volumes, making subsequent characterizations of these materials difficult. In future studies, larger-volume crucibles might be implemented for these heat treatments, which would require a larger volume of glass to be made up front. This was not considered in the current study due to the desire to for low-mass scoping tests to save on costs, chemicals, and time. Finally, the largest change in future studies related to this work will be informed by the chemical durability testing results that are still ongoing at ANL. If some of these samples show promise, more work could be done to explore similar compositions and, if some samples show poor chemical durability, they could be modified compositionally or simply eliminated from future work.

8.0 References

Ahmed, AA and SQ Mawlud. 2023. "Physical and optical properties of ternary lead-bismuth tellurite glass." *Heliyon* **9**:e16730.

Alzahrani, JS, A Hammoud, AS Altowyan, IO Olarinoye, AV Lebedev, and MS Al-Buriahi. 2023. "Influence of Sm/Bi substitution on synthesis, structural, and photon interaction properties of TeO single bond MoO_3 single bond BaO single bond Sm_2O_3 single bond Bi_2O_3 glass system." *Optik - International Journal for Light and Electron Optics* **274**:170507.

Bai, J, RK Brow, CW Kim, P Sandineni, and A Choudhury. 2021. "Redox effects on the structure and properties of Na-Mo-Fe phosphate glasses." *Journal of Non-Crystalline Solids* **557**:120573.

Brow, RK, CW Kim, and ST Reis. 2020. "Iron polyphosphate glasses for waste immobilization." *International Journal of Applied Glass Science* **11**(1):4-14.

Day, D, Z Wu, C Ray, and P Hrma. 1998. "Chemically Durable Iron Phosphate Glass Waste forms." *Journal of Non-Crystalline Solids* **241**(1):1-12.

Day, DE and CS Ray. 2013. *A Review of Iron Phosphate Glasses and Recommendations for Vitrifying Hanford Waste*. INL/EXT-13-30389, Idaho National Laboratory, Idaho Falls, ID.

Donze, S, L Montagne, and G Palavit. 2000. "Thermal conversion of heavy metal chlorides ($PbCl_2$, $CdCl_2$) and alkaline chlorides (NaCl, KCl) into phosphate glasses." *Chemistry of Materials* **12**(7):1921-25.

Donze, S, L Montagne, G Palavit, and G Antonini. 2001. "Structure and properties of phosphate glasses prepared from lead and cadmium chlorides." *Physics and Chemistry of Glasses* **42**(2):133-38.

Dwaikat, N, MI Sayyed, MHA Mhareb, M Dong, YSM Alajerami, I Alrammah, A Khalid, and MGB Ashiq. 2021. "Durability, optical and radiation shielding properties for new series of boro-tellurite glass." *Optik - International Journal for Light and Electron Optics* **245**:167667.

Ebert, WL. 2005. *Testing to Evaluate the Suitability of Waste Forms Developed for Electrometallurgically-Treated Spend Sodium-Bonded Nuclear Fuel for Disposal in the Yucca Mountain Repository*. ANL-05/43, Argonne National Laboratory-East, Argonne, IL.

Ebert, WL, BJ Riley, JA Peterson, and SM Frank. 2018. *Durability Testing of Developmental Iron Phosphate Waste Forms for Echem Salt Waste*. NTRD-MRWFD-2018-000513, Argonne National Laboratory, Lemont, IL.

Ersundua, AE, MI Sayyed, O Kıbrıslı, V Akıllı, and MÇ Ersundu. 2021. "A thorough investigation of the Bi_2O_3-$PbCl_2$-TeO_2 system: Glass forming region, thermal, physical, optical, structural, mechanical and radiation shielding properties." *Journal of Alloys and Compounds* **857**:158279.

Fredrickson, G. 2021. *Overview of Pyroprocessing for Reprocessing and Spent Fuel Treatment (ARPA-E Converting UNF Radioisotopes into Energy Workshop)*. INL/MIS-21-63449, Idaho National Laboratory, Idaho National Laboratory.

Frolova, AV, SA Fimina, and SE Vinokurov. 2023. "Immobilization of chloride radioactive waste using a phosphate glass composite material." *Atomic Energy* **134**:332–37.

Garino, TJ, TM Nenoff, JL Krumhansl, and DX Rademacher. 2011. "Low-Temperature Sintering Bi-Si-Zn-Oxide Glasses for Use in Either Glass Composite Materials or Core/Shell ^{129}I Waste Forms." *Journal of the American Ceramic Society* **94**(8):2412-19.

Gupta, N and A Khanna. 2018. "Glass and anti-glass phase co-existence and structural transitions in bismuth tellurite and bismuth niobium tellurite systems." *Journal of Non-Crystalline Solids* **481**:594-603.

Hammad, AH, AM Abdelghany, and HA ElBatal. 2017. "Thermal, Structural, and Morphological Investigations of Modified Bismuth Silicate Glass-Ceramics." *Silicon* **9**:239-48.

Hase, H, H Nasu, J Matsuoka, and K Kamiya. 1995. "Third-Order Optical Nonlinearity of LiX-Li_2O-TeO_2 and AgX-Ag_2O-TeO_2 (X=Cl, Br, I) Glasses." *Journal of the Ceramic Society of Japan* **103**(11):1117-21.

Hsu, J-H, JW Newkirk, C-W Kim, RK Brow, ME Schlesinger, CS Ray, and DE Day. 2014. "The performance of Inconel 693 electrodes for processing an iron phosphate glass melt containing 26wt.% of a simulated low activity waste." *Journal of Nuclear Materials* **444**(1):323-30.

Hsu, J-H, JW Newkirk, C-W Kim, CS Ray, RK Brow, ME Schlesinger, and DE Day. 2013. "Corrosion of Inconel 690 and Inconel 693 in an iron phosphate glass melt." *Corrosion Science* **75**:148-57.

Itas, YS, MM Nono, Y Trabelsi, IF Alshdoukhi, MR Alrahili, R Haldhar, and MK Hossain. 2024. "Significant improvement in the gamma ray attenuation properties of bismuth tellurite glass using molybdenum oxide reinforcement." *Progress in Nuclear Energy* **176**:105374.

Kang, HW, J-H Choi, KR Lee, and H-S Park. 2021. "Addition of transition metal oxides on silver tellurite glass for radioactive iodine immobilization." *Journal of Nuclear Materials* **543**:152635.

Kaur, N and A Khanna. 2014. "Structural characterization of borotellurite and alumino-borotellurite glasses." *Journal of Non-Crystalline Solids* **404**:116-23.

Ketterer, J and VK Freiburg. 1986. "Crystal structure of the bismuth silicate Bi_2SiO_5." *Neues Jahrbuch für Mineralogie (Journal of Mineralogy and Geochemistry)* **1**:13-18.

Kim, C-W and DE Day. 2003. "Immobilization of Hanford LAW in iron phosphate glasses." *Journal of Non-Crystalline Solids* **331**(1):20-31.

Kim, CW, CS Ray, D Zhu, DE Day, D Gombert, A Aloy, A Moguš-Milanković, and M Karabulut. 2003. "Chemically durable iron phosphate glasses for vitrifying sodium bearing waste (SBW) using conventional and cold crucible induction melting (CCIM) techniques." *Journal of Nuclear Materials* **322**(2):152-64.

Kozhukharov, V, M Marinov, and I Gugov. 1983. "A new family of tellurite glasses." *Journal of Materials Science* **18**:1557-63.

Kulikova, SA, SS Danilov, AV Matveenko, AV Frolova, KY Belova, VG Petrov, SE Vinokurov, and BF Myasoedov. 2021. "Perspective Compounds for Immobilization of Spent Electrolyte from Pyrochemical Processing of Spent Nuclear Fuel." *Applied Sciences* **11**(23):11180.

Lee, CW, J-Y Pyo, H-S Park, JH Yang, and J Heo. 2017. "Immobilization and bonding scheme of radioactive iodine-129 in silver tellurite glass." *Journal of Nuclear Materials* **492**:239-43.

Lere-Adams, AJ, MC Dixon Wilkins, D Bollinger, S Stariha, R Farzana, P Dayal, DJ Gregg, S Chong, BJ Riley, ZM Heiden, and JS McCloy. 2024. "Glass-bonded ceramic waste forms for immobilization of radioiodine from caustic scrubber wastes." *Journal of Nuclear Materials* **591**:154938.

Lere-Adams, AJ, N Stone-Weiss, DL Bollinger, and JS McCloy. 2022. "Scoping studies for low-temperature melting ZnO-Bi_2O_3-(B_2O_3, SiO_2) binder glass." *MRS Advances* **7**:90-94.

Li, H-W and S-Q Man. 2009. "Optical properties of Er^{3+} in MoO_3-Bi_2O_3-TeO_2 glasses." *Optics Communications* **282**(8):1579-83.

Ma, L, RK Brow, and ME Schlesinger. 2017. "Dissolution behavior of Na_2O-FeO-Fe_2O_3-P_2O_5 glasses." *Journal of Non-Crystalline Solids* **463**:90-101.

Marcial, J, S Chong, BJ Riley, RK Brow, JD Vienna, CW Kim, and M Tang. 2024. *Bonding Environments and Radiation Stabilities of Phosphate Glasses*. PNNL-35754, Pacific Northwest National Laboratory, Richland, WA.

McCloy, JS, BJ Riley, AS Lipton, CF Windisch, NM Washton, MJ Olszta, and CP Rodriguez. 2013. "Structure and Chemistry in Halide Lead–Tellurite Glasses." *The Journal of Physical Chemistry C* **117**(7):3456-66.

Mesko, MG, DE Day, and BC Bunker. 2000. "Immobilization of CsCl and SrF_2 in iron phosphate glass." *Waste Management* **20**(4):271-78.

Moschetti, TL, W Sinkler, T DiSanto, MH Novy, AR Warren, D Cummings, SG Johnson, KM Goff, KJ Bateman, and SM Frank. 2000. Characterization of a ceramic waste form encapsulating radioactive electrorefiner salt. Presented at *Scientific Basis for Nuclear Waste Management, XXIII*, pp. 577-82, Materials Research Society, Pittsburgh, PA.

Moustafa, YM. 1999. "Characterization of iron oxychloride potassium phosphate glasses." *Journal of Physics D: Applied Physics* **32**:2278–86.

Murray, P, H Werth, S Sullivan, BJ Riley, M Simpson, C Lonergan, and K Carlson. 2024. "Phosphate-based dechlorination of electrorefiner salt waste using a phosphoric acid precursor." *ACS Omega* **9**(17):19395-400.

Riley, BJ, NL Canfield, M Peterson, JL George, S Chong, and JV Crum. 2023a. *Crystalline versus Glassy Nature of Iron Phosphate Waste Forms Subjected to Different Slow Cooling Curves*. PNNL-34917, Pacific Northwest National Laboratory, Richland, WA.

Riley, BJ and S Chong. 2021. "Effects of composition and canister centerline cooling on microstructure, phase distribution, and chemical durability of dehalogenated iron phosphate waste forms." *Journal of Non-Crystalline Solids* **579**:121319.

Riley, BJ and S Chong. 2020. "Glass waste form options for rare-earth fission products from electrochemical reprocessing." *Journal of Non-Crystalline Solids* **545**:120161.

Riley, BJ, S Chong, and CE Lonergan. 2021. "Dechlorination Apparatus for Treating Chloride Salt Wastes: System Evaluation and Scale-Up." *ACS Omega* **6**(47):32239-52.

Riley, BJ, S Chong, and ET Nienhuis. 2023b. *Canister Centerline Cooling Experiments for DPF5-336 Reference Material Made with ERV3b Salt Simulant*. PNNL-33802, Pacific Northwest National Laboratory, Richland, WA.

Riley, BJ, S Chong, M Peterson, and ET Nienhuis. 2023c. *Aluminophosphate Waste Forms for Immobilizing Cations from Electrochemical Salt Wastes*. PNNL-33906, Pacific Northwest National Laboratory, Richland, WA.

Riley, BJ, JO Kroll, JA Peterson, DA Pierce, WL Ebert, BD Williams, MMV Snyder, SM Frank, JL George, and K Kruska. 2017a. "Assessment of lead tellurite glass for immobilizing electrochemical salt wastes from used nuclear fuel reprocessing." *Journal of Nuclear Materials* **495**:405-20.

Riley, BJ, JA Peterson, JD Vienna, WL Ebert, and SM Frank. 2020. "Dehalogenation of electrochemical processing salt simulants with ammonium phosphates and immobilization of salt cations in an iron phosphate glass waste form." *Journal of Nuclear Materials* **529**:151949.

Riley, BJ, BT Rieck, JV Crum, J Matyáš, J McCloy, SK Sundaram, and JD Vienna. 2010. *Alternative Electrochemical Salt Waste Forms, Summary of FY2010 Results*. FCRD-WAST-2010-000129, PNNL-19690, Pacific Northwest National Laboratory, Richland, WA.

Riley, BJ, BT Rieck, JS McCloy, JV Crum, SK Sundaram, and JD Vienna. 2012. "Tellurite glass as a waste form for mixed alkali-chloride waste streams: candidate materials selection and initial testing." *Journal of Nuclear Materials* **424**(1-3):29-37.

Riley, BJ, JD Vienna, SM Frank, JO Kroll, JA Peterson, NL Canfield, Z Zhu, J Zhang, K Kruska, and DK Schreiber. 2017b. "Glass binder development for a glass-bonded sodalite ceramic waste form." *Journal of Nuclear Materials* **489**:42-63.

Shin, S-S, G-Y Kim, B Lee, J-H Yang, Y-S Son, J-H Choi, J-Y Pyo, KR Lee, H-S Park, and HW Kang. 2024. "Silver tungstate–tellurite glass for radioactive iodine immobilization." *Journal of Non-Crystalline Solids* **624**:122728.

Siemer, DD. 2012. "Improving the integral fast reactor's proposed salt waste management system." *Nuclear Technology* **178**(3):341-52.

Tanaka, K, T Yoko, H Yamada, and K Kamiya. 1988. "Structure and Ionic Conductivity of LiCl-Li_2O-TeO_2 Glass." *Journal of Non-Crystalline Solids* **103**:250-56.

Udovic, M, P Thomas, A Mirgorodsky, O Durand, M Soulis, O Masson, T Merle-Méjean, and JC Champarnaud-Mesjard. 2006. "Thermal characteristics, Raman spectra and structural properties of new tellurite glasses within the Bi_2O_3-TiO_2-TeO_2 system." *Journal of Solid State Chemistry* **179**:3252–59.

Werth, H, J Beland, P Murray, D Liang, L Sharpless, J Evarts, C Lonergan, BJ Riley, M Simpson, and K Carlson. 2025. "Evaluation of Processing Conditions for the Reduction of Electrochemical Salt Waste Using Phosphate-Based Dechlorination." *ACS ES&T Engineering*:10.1021/acsestengg.5c00396.

Xu, T, F Chen, S Dai, X Shen, X Wang, Q Nie, C Liu, K Xu, and J Heo. 2011. "Glass formation and third-order optical nonlinear properties within TeO_2-Bi_2O_3-BaO pseudo-ternary system." *Journal of Non-Crystalline Solids* **357**:2219–22.

Zamyatin, OA, AD Plekhovich, EV Zamyatina, and AA Sibirkin. 2016. "Glass-forming region and physical properties of the glasses in the TeO_2-MoO_3-Bi_2O_3 system." *Journal of Non-Crystalline Solids* **452**:130-35.

Zhao, G, Y Tian, H Fan, J Zhang, and L Hu. 2013. "Properties and Structures of Bi_2O_3-B_2O_3-TeO_2 Glass." *Journal of Materials Science & Technology* **29**(3):209-14.

Pacific Northwest National Laboratory

902 Battelle Boulevard
P.O. Box 999
Richland, WA 99354

1-888-375-PNNL (7665)

www.pnnl.gov